EVALUATION FRAMEWORK FOR CISLUNAR SPACE DOMAIN AWARENESS (SDA) SYSTEMS

THESIS

Simon R. Knister, Captain, USAF

AFIT-ENV-MS-20-M-221

DEPARTMENT OF THE AIR FORCE
AIR UNIVERSITY

AIR FORCE INSTITUTE OF TECHNOLOGY

Wright-Patterson Air Force Base, Ohio

AFIT-ENV-MS-20-M-221

EVALUATION FRAMEWORK FOR CISLUNAR SPACE DOMAIN AWARENESS (SDA) SYSTEMS

THESIS

Presented to the Faculty

Department of Systems Engineering and Management

Graduate School of Engineering and Management

Air Force Institute of Technology

Air University

Air Education and Training Command

In Partial Fulfillment of the Requirements for the

Degree of Master of Science in Systems Engineering

Simon R. Knister, BS

Captain, USAF

February 2019

AFIT-ENV-MS-20-M-221

EVALUATION FRAMEWORK FOR CISLUNAR SPACE DOMAIN AWARENESS (SDA) SYSTEMS

Simon R. Knister, BS

Captain, USAF

Committee Membership:

Lt Col B. D. Little, PhD
Chair

Lt Col K. W. Johnson, PhD
Member

Dr. J. M. Colombi
Member

Lt Col A. M. Cox, PhD
Member

Acknowledgments

First, I would like to thank the scientific giants on whose shoulders we all stand. From Kepler, Newton, and Szebehely, to Dr. Howell and the many, many geniuses at NASA. The more I learn about astrodynamics, the more I realize how little I know.

To my research advisors, Lt Col Johnson and Lt Col Little, thank you for your patience and guidance through this endeavor. I sincerely appreciate your willingness to take a Systems Engineering student under your wings, and to mentor me as an astronautical engineer. I would not have made it to cislunar space without your help.

Finally, to my loving wife, you inspire me to continue to reach for the stars. Your steadfast devotion pushed me through each late night of studying, coding, and writing. Thank you for your support and sacrifice throughout this journey.

Capt Simon Knister

Table of Contents

Page

List of Tables

List of Figures

Abstract

Modern space missions are increasingly transiting cislunar space, requiring expansion of existing Space Traffic Management (STM) functions. Legacy Space Domain Awareness (SDA) systems were not purpose-built to detect and track cislunar objects, which could require acquisition of a new system of systems. There are numerous parameters that could be varied for each system, as well as the type and location of systems across the architecture. This research attempts to solve this problem by applying a model-based systems engineering (MBSE) approach to assess the performance and financial burden of a given system of systems. Fitness metrics are developed based upon the ability of an architecture to detect and track a cislunar object, as well as the aggregate cost of that system. The physics of the cislunar SDA domain are examined, and solar exclusion angles, solar phase angle, and lunar exclusion angles are determined to play a large role in determining system performance. For the selected reference architecture, consisting of a single satellite in an L1 Lyapunov orbit, performance is dominated by lunar exclusion angles. This physical effect renders ground-based observers useless, although space-based observers are still capable of viewing the object of interest when the Earth blocks the Moon from the sensor field of view. The highest performing architecture is determined to be a 4-ball synodic plane-matched LEO architecture.

EVALUATION FRAMEWORK FOR CISLUNAR SPACE SITUATIONAL AWARENESS (SDA) SYSTEMS

I. Introduction

1.1 Background.

In recent decades, the eyes of the world have risen back to the Moon and the cislunar space between it and the Earth. In the civil sector, missions such as the NASA Lunar Orbital Platform-Gateway may begin to occupy Earth-Moon Lagrange points as early as 2022 to provide logistical support for human exploration (NASA, 2018). Commercial entities are exploring lunar-mined fuel to extend the operating lives of satellites (Vedda, 2018). Established space-faring nations such as China and Russia are also planning and executing missions within cislunar space (Bartels, 2019). Even burgeoning space powers such as Israel and India are transiting cislunar space with the dreams of landing on the moon with their Beresheet (Wall, 2019) and Chandrayaan-2 (Regan and Pokharel, 2019) systems. In spite of the increased interest in cislunar operations, the United States and the community of nations at large do not have a dedicated Space Domain Awareness (SDA) system to enable Space Traffic Management (STM) functions to ensure safety of flight and peace of operations in this regime. Along these lines, the importance of monitoring this regime was emphasized by Major General Shaw when he was the Vice Commander of Air Force Space Command (Hitchens, 2019).

Multiple SDA architectures could fulfill this role, each with varying sensing phenomenology, sensor sizes, number of systems, system basing, and other parameters—too many to evaluate one at a time. The Space Development Agency aims to provide STM

functions for cislunar space; however, they have prescribed a LEO constellation without consideration for other sensor basing locations (Hitchens, 2019). In practice, the sensors of the US Space Surveillance Network (SSN) act as an integrated system of systems to support STM functions for objects in the Earth's gravitational sphere of influence. The design of an SDA architecture that meets the system of systems requirements necessitates a more holistic, top-down approach. Applying a model-based systems engineering (MBSE) framework, which INCOSE defined as "the formalized application of modeling to support system requirements, design, analysis" (INCOSE, 2007) will allow the evaluation of SDA architectures for STM of cislunar objects.

Although the requirements for a cislunar SDA architecture are not yet defined, they would be conceptually similar to SDA for near-Earth orbits. S*pace Policy Directive 3* (Office of the POTUS, 2018) defines STM as "the planning, coordination, and on-orbit synchronization of activities to enhance the safety, stability, and sustainability of operations in the space environment" and SDA as "the knowledge and characterization of space objects and their operational environment to support safe, stable, and sustainable space activities". Given that the majority of SDA functions for the United States are performed by the Department of Defense, it is useful to examine *Joint Publication 3-14, Space Operations* (US JCS 2018), which functionally decomposes SDA into "detect/track/identify, integrated tactical warning, and attack assessment and characterization". This research will focus on a framework for evaluating the ability of an SDA architecture to perform detect and track functions in support of STM.

1.2 SDA in Cislunar Space.

There are two major differences between SDA for Earth orbit vs. cislunar space. The first is the gravitational impact of the Moon on orbital trajectories and operations as satellites traverse and operate externally to the Earth's sphere of influence (SOI). Within the Earth's SOI, simple Hohmann transfers can be used to plan impulsive orbital maneuvers. However, in cislunar space these transfers are driven by the combined gravitational fields of the Earth and Moon. This affects the algorithms that SDA sensors use for developing satellite tracks, which typically center on orbit determination as opposed to real-time custody.

The second is range losses and search volume; to quote *The Hitchhiker's Guide to the Galaxy*, "Space is big. You just won't believe how vastly, hugely, mind-bogglingly big it is" (Adams, 1980). This has demonstrated technical challenges for civil, military, and commercial systems for geosynchronous orbit (GEO) systems, as most applications are vexed by range-induced inverse square laws. But these challenges pale in comparison to the range impacts of cislunar observations, which operate in ranges that are more than nine times larger than GEO. This results in both increased volume over which to search for and discover a given satellite, as well as significantly increased range losses.

Due to the range losses implicit with cislunar SDA, certain sensor types will be precluded. Free space propagation losses for RADAR systems are inversely proportional to the quartic of the range, and will therefore be excluded from this analysis. Passive detection using cooperative ranging and tracking will also be precluded, as such a system does not exist at large for space faring nations. Therefore, the architecture will be composed

solely of electro-optic SDA sensors, whose signal diminishes proportionally only to the square of distance.

Another simplifying assumption for this research pertains to the objects that the SDA architectures must observe. The evaluated capability of a given cislunar SDA architecture is dependent upon the set of cislunar objects that it is tasked to observe. There could be multiple objects, orbiting any of the five Lagrange points or merely transiting cislunar space, in any of an infinite number of orbits or trajectories. The scenario for this research is simple, consisting of a single object in an L_1 Lyapunov orbit in the Earth-Moon system.

1.3 Thesis Overview

The objectives of this research are three-fold: The first is to understand the physical implications of cislunar space, specifically the L_1 point, on assessing SDA architectures, and to develop "fitness" parameters to quantify the ability of a given SDA architecture to detect and track cislunar objects. The second is to develop a corresponding integrated model with which to evaluate these fitness parameters. The third is to assess various SDA architectures and provide recommendations for future system acquisitions by the United States Government.

Achieving these objectives requires that the following research questions be answered:

1. What are the measures for determining the "fitness" of a given SDA architecture for detecting and tracking cislunar satellites?

2. How can MBSE support evaluation of SDA architectures for detecting and tracking cislunar satellites?
3. How do optimized GEO SDA architectures compare to potential cislunar SDA architectures for detecting and tracking cislunar satellites when accounting for system cost?

The remainder of this thesis is organized as follows:

Chapter 2 – Background: Means for creating cislunar orbits are explored. Physics of SDA systems are reviewed. MBSE approaches for modeling SDA systems are explored.

Chapter 3 – Methodology: The MBSE tool is developed within a MATLAB and STK model. Test cases are developed, both to understand the implications of the cislunar environment and to compare various SDA architectures.

Chapter 4 – Analysis and Results: Results of test cases are analyzed for implications and trends. The test SDA architectures are compared to determine which is best.

Chapter 5 – Conclusions and Recommendations: The thesis concludes with final commentary on the analysis, as well as recommendations for future research using this study as a foundation.

II. Background

2.1 Chapter Overview

Knowledge of three technical areas is required for development of a framework for cislunar SDA architecture evaluation: (1) dynamics of the cislunar environment, (2) physics of SDA systems, and (3) SDA architecture evaluation techniques. This chapter begins with a background on the generation of libration-point orbits, from the classical Circular Restricted Three Body Problem (CR3BP) through first-order approximations of libration orbits, to the generation of more realistic orbits using the multiple-shooting method. This is followed by an overview of SDA systems, including basic sensor physics and the impacts of the time-dependent geometries of the celestial bodies. This is concluded by a review of evaluation techniques for SDA architectures.

2.2 Dynamics of the cislunar environment

Compared to objects operating solely within the Earth's gravitational SOI, the dynamics of objects operating in the cislunar environment are driven by gravitational effects of both the Earth and Moon. This means that instead of the traditional two-body problem, which leads to closed-form analytical equations of motion, the three-body problem must be used. These equations have not yet been solved analytically, and require numerical solutions to dynamics problems. To further simplify the dynamics, additional assumptions are made using the Circular Restricted Three Body Problem (CR3BP).

2.2.1. The Circular Restricted Three Body Problem (CR3BP)

The CR3BP makes several simplifying assumptions regarding the dynamics of three-body systems. These assumptions are as follows (Parker and Anderson, 2013):

1) Satellite mass is infinitesimally small compared to the primary masses, and is therefore considered massless
2) The only forces acting on the satellite are the gravitational forces from the two massive bodies
3) The two primary objects are in circular motion about their barycenter

These assumptions permit definition of a rotating reference frame centered at the synodic barycenter, which is the center of mass for the system. The x-axis points toward the smaller primary, the y-axis lies on the synodic plane, perpendicular to the x-axis, and the z-axis completes the primary axes. Note that some sources, such as Wiesel (2010), place the larger primary in the direction of the positive x-axis. It is therefore very important to review the coordinate frame being used in a given work.

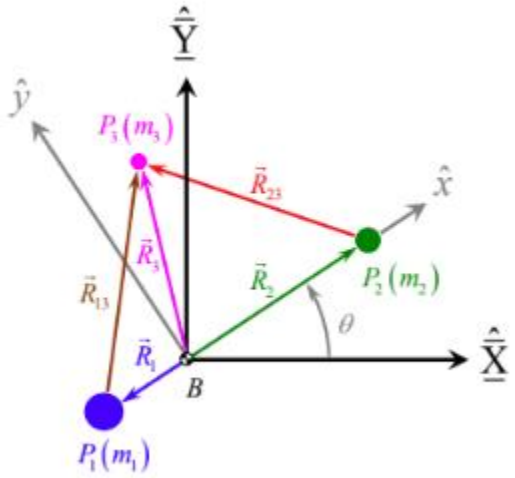

Figure 1: The Three Body Problem (adapted from Grebow, 2006)

Applying Newton's Second Law to the 3-body problem in the inertial frame yields the following dynamics equation

$$m_3 \frac{{}^{I}d^2\vec{R}_3}{dt^2} = -\frac{Gm_3m_1}{\left\|\vec{R}_{13}\right\|^3}\vec{R}_{13} - \frac{Gm_3m_2}{\left\|\vec{R}_{23}\right\|^3}\vec{R}_{23} \quad (1)$$

which can be simplified using a set of characteristic quantities which can be used to non-dimensionalize the equations, defined as follows (Grebow, 2006):

Characteristic Length: $l^* = \left\|\vec{R_1}\right\| + \left\|\vec{R_2}\right\|$

Characteristic Mass: $m^* = m_1 + m_2$

Characteristic Time: $t^* = \sqrt{\frac{{l^*}^3}{Gm^*}}$

Note that by defining these quantities as such, the subsequent angular rate of the synodic frame with respect to the inertial frame, $\vec{\omega}^{BI}$, is equal to unity (Grebow, 2006).

Using the natural parameters in Appendix A, the characteristic quantities for the Earth-Moon system are as follows:

l^* (km)	m^* (kg)	t^* (days)
384,400	6.0368×10^{24}	4.3425

Table 1: Characteristic quantities for the Earth-Moon system

Substituting these terms into the 3-body equation yields

$$\frac{{}^{I}d^2\vec{r}_3}{d\tau^2} = -\frac{1-\mu}{\|\vec{r}_{13}\|^3}\vec{r}_{13} - \frac{\mu}{\|\vec{r}_{23}\|^3}\vec{r}_{23} \quad (2)$$

where

$$\vec{r}_3 = \frac{\vec{R}_3}{l^*}, r_{13} = \left\| \frac{\vec{R}_{13}}{l^*} \right\|, r_{23} = \left\| \frac{\vec{R}_{23}}{l^*} \right\| \tag{3}$$

and, the mass ratio μ is defined as $\mu = \frac{m_2}{m^*}$, and $\tau = \frac{t}{t^*}$ (Grebow, 2006).

To define the kinematics of the equation requires the application of the transport theorem, where the rotation of the synodic frame with respect to the inertial frame is defined as $\vec{\omega}^{BI}$.

Given that the rotation of the synodic frame, $\vec{\omega}^{BI}$, is equal to unity, the above can be simplified into the following three equations of motion in the synodic frame:

$$\ddot{x} - 2\dot{y} - x = -\frac{(1-\mu)(x-\mu)}{r_{13}^3} - \frac{\mu(x+(1-\mu))}{r_{23}^3} \tag{4}$$

$$\ddot{y} + 2\dot{x} - y = -\frac{(1-\mu)y}{r_{13}^3} - \frac{\mu y}{r_{23}^3} \tag{5}$$

$$\ddot{z} = -\frac{(1-\mu)z}{r_{13}^3} - \frac{\mu z}{r_{23}^3} \tag{6}$$

2.2.2. Equilibrium Points

One useful set of solutions to the CR3BP is the set of equilibrium points, also known as libration points (Grebow, 2006). These are points in space where the velocity and acceleration of an object are theoretically equal to zero. These equilibrium points provide a point at which a spacecraft could “hover” in place with respect to the primaries, which has useful applications for a variety of logistics, communication, and scientific missions.

Calculation of these points begins with setting the acceleration and velocity components of the equations of motion to zero, which yields the equations below:

$$x = -\frac{(1-\mu)(x+\mu)}{r_{13}^3} - \frac{\mu(x-(1-\mu))}{r_{23}^3} \tag{7}$$

$$y = -\frac{(1-\mu)y}{r_{13}^3} - \frac{\mu y}{r_{23}^3} \tag{8}$$

$$0 = -\frac{(1-\mu)z}{r_{13}^3} - \frac{\mu z}{r_{23}^3} \tag{9}$$

This uncovers a z-component that is decoupled from the x- and y-components, and which has a solution of $z = 0$. This reveals that the libration points lie in the synodic plane. The first three equilibrium points are discovered by setting $y=0$, which leaves

$$x = -\frac{(1-\mu)}{(x+\mu)^2} - \frac{\mu(x-1+\mu)}{(x-1+\mu)^2} \tag{10}$$

This equation may be solved using an iterative process, and results in the three collinear points (L_1, L_2, and L_3). The final two points (L_4, and L_5) are solved by setting $\left\|\vec{r}_{13}\right\| = \left\|\vec{r}_{23}\right\| = 1$, which provides a solution of

$$(x, y) = \left(\frac{1}{2} - \mu, \pm\frac{\sqrt{3}}{2}\right) \tag{11}$$

These points are commonly called the equilateral points, as they lie on the vertices of equilateral triangles with bases established by the two primary masses.

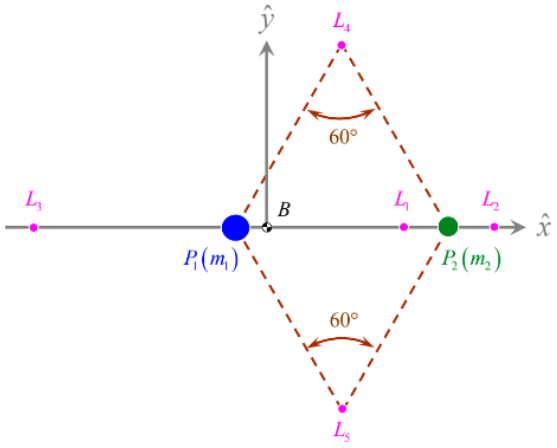

Figure 2: The CR3BP (adapted from Grebow, 2006)

Using the natural parameters in Appendix A, the Libration Points for the Earth-Moon system are as follows:

Libration Point	**x**	**y**
L_1	0.836915	0
L_2	1.155682	0
L_3	-1.005063	0
L_4	0.487849	0.866025
L_5	0.487849	-0.866025

Table 2: Libration points for the Earth-Moon system (non-dimensional units)

In practice, none of the equilibrium points in the Earth-Moon system are stable. While the L_4 and L_5 points are theoretically stable in the CR3BP, they are unstable in practice due to solar gravity-induced perturbations (Wiesel, 2010). Meanwhile, the collinear L_1, L_2, and L_3 points are unstable even in the theoretical CR3BP (Parker and Anderson, 2013). If a satellite were stationed at one of these points, the lack of stability means that a small

perturbation in initial conditions will cause the satellite to drift away from the libration point. This has driven researchers to investigate other solutions to the CR3BP, including periodic and semi-periodic orbits around the libration points.

2.2.3. First-order Analytic Solutions to the CR3BP

There are many families of periodic and semi-periodic orbits in the CR3BP. This research focuses on one type of orbit: The Lyapunov Orbits for the collinear L_1 point. As derived in Grebow (2006), the linearized first order approximation of the equations of motion yields the following for a Lissajous trajectory, where primes note a linear transformation about one of the equilibrium points, such that the origin of the prime coordinate frame is the L_1 or L_2 point:

$$x' = \frac{A_{y'}}{\beta_3} cos(s\tau + \phi) \tag{12}$$

$$y' = -A_{y'} sin(s\tau + \phi) \tag{13}$$

$$z' = A_{z'} sin(\nu\tau + \psi) \tag{14}$$

where $A_{y'}$ and $A_{z'}$ are orbital amplitudes of a Lissajous orbit in the y' and z' directions, and

$$\beta_3 = \frac{s^2 + U_{xx}eq}{2s} \tag{15}$$

$$\nu = \sqrt{|U_{zz}eq|} \tag{16}$$

$$s = \sqrt{\beta_1 + (\beta_1^2 + \beta_2^2)^{\frac{1}{2}}} \tag{17}$$

where s and ν are orbital frequencies of a Lissajous orbit in the x-y plane and z axis, and

$$\beta_1 = 2 - \frac{U_{xx}eq + U_{yy}eq}{2} \tag{18}$$

$$\beta_2^2 = -U_{xx}eqU_{yy}eq > 0 \tag{19}$$

The values U_{xx} and U_{yy} are the second partial derivatives of the pseudo-potential function U, which is defined as

$$U = \frac{1-\mu}{r_{13}} + \frac{\mu}{r_{23}} + \frac{1}{2}(x^2 + y^2) \tag{20}$$

$$U_{XX} = 1 - \frac{1-\mu}{r_{13}^3} + 3\frac{(x+\mu)^2(1-\mu)}{r_{13}^5} - \frac{\mu}{r_{23}^3} + 3\frac{\left(x-(1-\mu)\right)^2\mu}{r_{23}^5} \tag{21}$$

$$U_{YY} = 1 - \frac{1-\mu}{r_{13}^3} + 3\frac{y^2(1-\mu)}{r_{13}^5} - \frac{\mu}{r_{23}^3} + 3\frac{y^2\mu}{r_{23}^5} \tag{22}$$

$$U_{ZZ} = -\frac{1-\mu}{r_{13}^3} + 3\frac{z^2(1-\mu)}{r_{13}^5} - \frac{\mu}{r_{23}^3} + 3\frac{z^2\mu}{r_{23}^5} \tag{23}$$

Evaluating these equations for r_{13} and r_{23} at L_1 and L_2 yields the following:

$$U_{XX}(x_{eq}, 0,0) = 1 + 2\frac{1-\mu}{|x+\mu|^3} + 2\frac{\mu}{|x-(1-\mu)|^3} \tag{24}$$

$$U_{YY}(x_{eq}, 0,0) = 1 - \frac{1-\mu}{|x+\mu|^3} - \frac{\mu}{|x-(1-\mu)|^3} \tag{25}$$

$$U_{ZZ}(x_{eq}, 0,0) = -\frac{1-\mu}{|x+\mu|^3} - \frac{\mu}{|x-(1-\mu)|^3} \tag{26}$$

where x_{eq} is the x-position of the L_1 or L_2 points in the barycentric coordinate system.

This enables calculation of the following values for β_3, s, and ν using the values for L_1 and L_2 from Table 2:

	β_3	s	ν
L_1	3.5865	2.3344	2.2688
L_2	2.9126	1.8626	1.7862

Table 3: Parameters for L_1 and L_2 Lyapunov and Lissajous Orbits

Using initial values of $A_{y'} = 15{,}000$ km and $A_{z'} = 20{,}000$ km with $\phi = 180°, \psi = 0°$ generates the following Lissajous trajectory over ten orbits. The form of this orbit with $A_{z'} = 0$ km is called a Lyapunov orbit, and is simply the projection of a Lissajous orbit onto the x-y plane as depicted in the top-left quadrant.

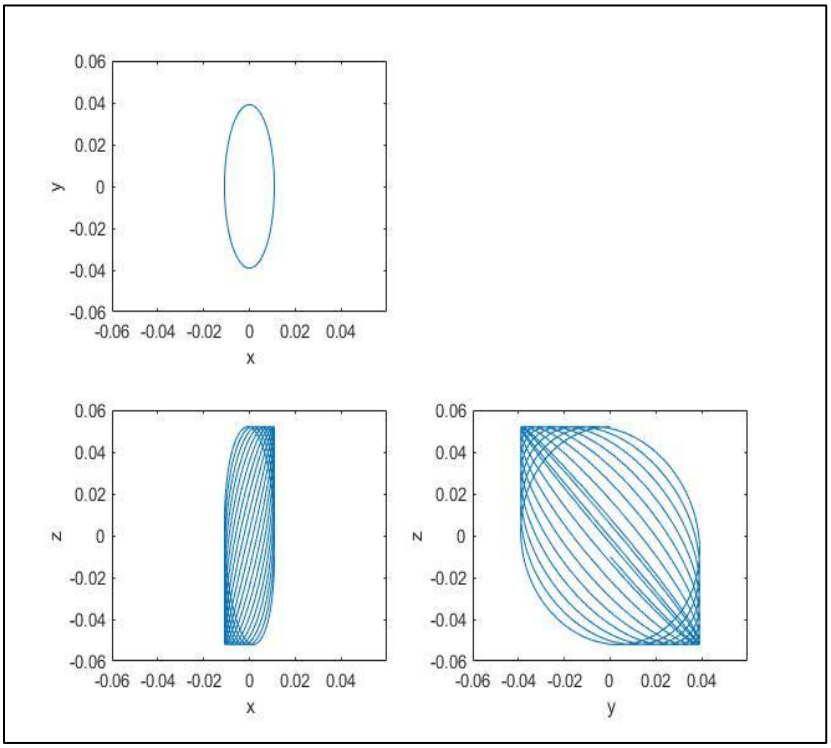

Figure 3: Lissajous orbit centered at the L_1 point for $\boldsymbol{A_{y'}} = 15{,}000$ km and $\boldsymbol{A_{z'}} = \boldsymbol{20{,}000}$km with $\boldsymbol{\phi = 180°, \psi = 0°}$ over ten orbits. Units are dimensionless.

This section developed first-order linearized approximations to Lissajous and Lyapunov orbits. Under higher-order CR3BP propagation, these equations of motion do not hold true. However, they do produce initial conditions as an input to a numerical estimator for Lissajous and Lyapunov orbits in the CR3BP. The following sections will describe the process of developing an L_1 Lyapunov orbit.

2.2.4. The State Transition Matrix (STM)

To develop the semi-periodic orbits under the non-linear model and in the presence of other perturbations and forces requires an understanding of orbital perturbations due to variations in initial conditions. This will be enabled by the State Transition Matrix (STM), which is a set of matrix equations composed of partial derivatives of the satellite state. This matrix, $\boldsymbol{\Phi}$, represents the variations in satellite state at time τ as a result of initial conditions at time τ_0:

$$\boldsymbol{\Phi}(\tau,\tau_0)=\frac{\delta \boldsymbol{X}(\tau)}{\delta \boldsymbol{X}(\tau_0)}=\begin{bmatrix} \frac{\delta x}{\delta x_0} & \frac{\delta x}{\delta y_0} & \frac{\delta x}{\delta z_0} & \frac{\delta x}{\delta \dot{x}_0} & \frac{\delta x}{\delta \dot{y}_0} & \frac{\delta x}{\delta \dot{z}_0} \\ \frac{\delta y}{\delta x_0} & \frac{\delta y}{\delta y_0} & \frac{\delta y}{\delta z_0} & \frac{\delta y}{\delta \dot{x}_0} & \frac{\delta y}{\delta \dot{y}_0} & \frac{\delta y}{\delta \dot{z}_0} \\ \frac{\delta z}{\delta x_0} & \frac{\delta z}{\delta y_0} & \frac{\delta z}{\delta z_0} & \frac{\delta z}{\delta \dot{x}_0} & \frac{\delta z}{\delta \dot{y}_0} & \frac{\delta z}{\delta \dot{z}_0} \\ \frac{\delta \dot{x}}{\delta x_0} & \frac{\delta \dot{x}}{\delta y_0} & \frac{\delta \dot{x}}{\delta z_0} & \frac{\delta \dot{x}}{\delta \dot{x}_0} & \frac{\delta \dot{x}}{\delta \dot{y}_0} & \frac{\delta \dot{x}}{\delta \dot{z}_0} \\ \frac{\delta \dot{y}}{\delta x_0} & \frac{\delta \dot{y}}{\delta y_0} & \frac{\delta \dot{y}}{\delta z_0} & \frac{\delta \dot{y}}{\delta \dot{x}_0} & \frac{\delta \dot{y}}{\delta \dot{y}_0} & \frac{\delta \dot{y}}{\delta \dot{z}_0} \\ \frac{\delta \dot{z}}{\delta x_0} & \frac{\delta \dot{z}}{\delta y_0} & \frac{\delta \dot{z}}{\delta z_0} & \frac{\delta \dot{z}}{\delta \dot{x}_0} & \frac{\delta \dot{z}}{\delta \dot{y}_0} & \frac{\delta \dot{z}}{\delta \dot{z}_0} \end{bmatrix} \tag{27}$$

which satisfies the following differential equation

$$\dot{\boldsymbol{\Phi}}(\tau,\tau_0)=\boldsymbol{A}(\tau)\boldsymbol{\Phi}(\tau,\tau_0) \tag{28}$$

where

$$\boldsymbol{A}(\tau)=\frac{\delta\dot{\boldsymbol{X}}(\tau)}{\delta\boldsymbol{X}(\tau)} \tag{29}$$

For the CR3BP, this term is equal to (Parker and Anderson, 2013)

$$\boldsymbol{A}(\tau)=\begin{bmatrix}0 & \boldsymbol{I}\\ \boldsymbol{U_{XX}} & 2\boldsymbol{\Omega}\end{bmatrix} \tag{30}$$

where

$$\boldsymbol{\Omega}=\begin{bmatrix}0 & 1 & 0\\ -1 & 0 & 0\\ 0 & 0 & 0\end{bmatrix} \tag{31}$$

and $\boldsymbol{U_{XX}}$, the matrix of second partial derivatives of the pseudo-potential matrix ,$\boldsymbol{U}$, with respect to the satellite's position is

$$\boldsymbol{U_{XX}}=\begin{bmatrix}\frac{\delta\ddot{x}}{\delta x} & \frac{\delta\ddot{x}}{\delta y} & \frac{\delta\ddot{x}}{\delta z}\\ \frac{\delta\ddot{y}}{\delta x} & \frac{\delta\ddot{y}}{\delta y} & \frac{\delta\ddot{y}}{\delta z}\\ \frac{\delta\ddot{z}}{\delta x} & \frac{\delta\ddot{z}}{\delta y} & \frac{\delta\ddot{z}}{\delta z}\end{bmatrix} \tag{32}$$

This matrix can be developed by calculating the partial derivatives of the equations of motion for the CR3BP. In practice, the state transition matrix is calculated by developing the matrix $\boldsymbol{A}(\tau)$, and numerically integrating the equations of motion using the initial conditions at τ_0 to calculate $\boldsymbol{\Phi}(\tau,\tau_0)$.

2.2.5. Developing L_1 Lyapunov Orbits in the CR3BP

Calculation of the Lyapunov orbits around the collinear points leverages the fact that periodic motion around these points is symmetric across the x-z plane. First, the initial state

vector lying upon the x-axis, whose parameters are calculated from the first-order linearized approximation to the orbit, is defined as

$$\dot{X}_0 = \begin{bmatrix} x_0 \\ 0 \\ 0 \\ \dot{y}_0 \\ 0 \\ 0 \end{bmatrix} \tag{33}$$

These initial conditions must be modified such that the subsequent crossing of the x-z plane yields a velocity in the y-direction of zero, which assures symmetry.

There are several means of doing this, such as simple shooting (Ostman, 2019, and Grebow, 2006) and differential correction (Parker and Anderson, 2013, and AGI, 2019). Each of these techniques entail iteratively propagating the trajectory using the State Transition Matrix, comparing the end state to the desired end state, and varying control parameters until the velocity in the y-direction is below a desired threshold value. The example trajectory below for $A_{y'} = 15{,}000$ km and $A_{z'} = 0$ km with $\phi = 180°, \psi = 0°$ was developed using STK's Astrogator tool.

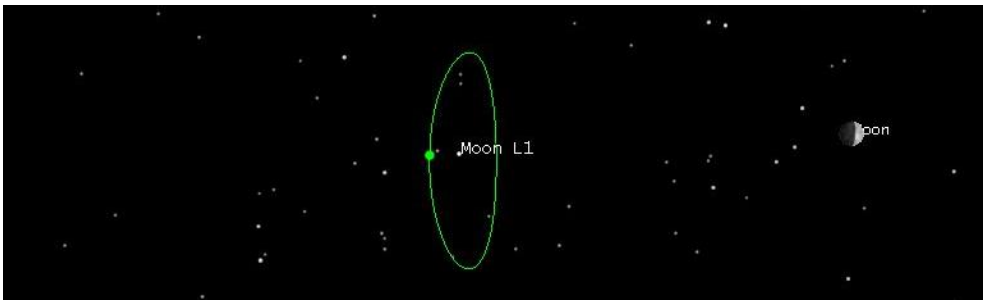

Figure 4: Lyapunov orbit in STK for $\boldsymbol{A_{y'} = 15{,}000}$ km and $\boldsymbol{A_{z'} = 0}$ km with $\boldsymbol{\phi = 180°, \psi = 0°}$

2.3 Overview of SDA systems

There are three categories of sensors that are used for SDA: Radar, cooperative tracking signals, and electro-optic. Radar systems have a range loss term proportional to propagation distance to the fourth (NAVWAR 2013), which makes traditional terrestrial systems impractical for GEO SDA, let alone cislunar SDA (Wiesel, 2010). Traditional deep space ranging systems such as the NASA Deep Space Network (DSN) require cooperative spacecraft behavior that leverages sequential ranging or pseudo-noise (PN) ranging signals, both of which require cooperation from the object being tracked (NASA, 2009). This may not be a reasonable expectation for all objects and situations. Therefore, this research assumes an architecture comprised entirely of electro-optic sensors.

Electro-optic systems detect optical signals reflected from the satellite of interest towards a telescope. These systems can be both ground-based (e.g., GEODSS, SST) and space-based (e.g., SBSS, ORS-5) (Ackermann, et al., 2015).

2.3.1. Signal Chain for Electro-Optic SDA Systems

The objective of electro-optic SDA systems is to collect and digitize electromagnetic radiation from the Sun, typically in the visible spectrum, which is reflected by the satellite of interest towards the sensor as depicted in the diagram below. For ground based sensors, there are additional losses as the reflected light propagates through the atmosphere. Once in the optical chain of the sensor, there are additional losses and noise terms that take away from the signal term.

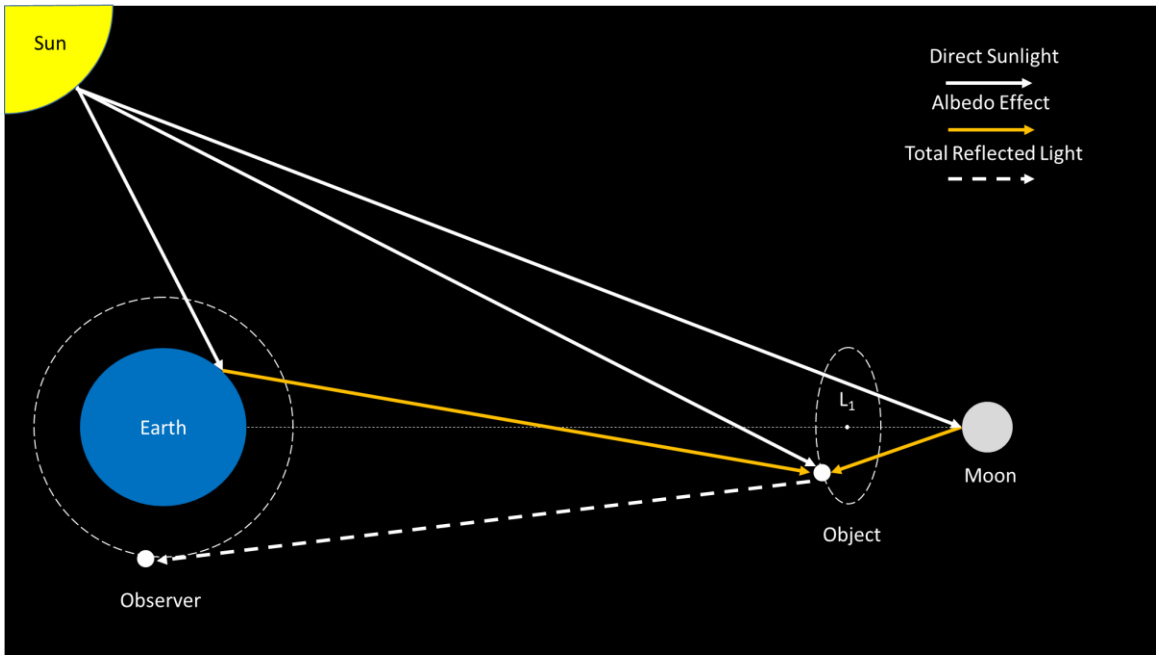

Figure 5: Optical signal chain for SDA (not to scale)

Signal Source. The first term in the signal budget is the signal source, which is light from the Sun, which reaches the average orbital radius of the Earth with a radiance of $S = 1366.1 Wm^{-2}$ (Pisacane, 2016). While this value would vary for objects not located at the Earth's surface, it is a small fractional difference for objects between the Earth and the Moon and is not worth taking into account for this research. Therefore, this value can be used for the solar radiance directly incident upon a cislunar object.

Albedo Effect. In addition to solar radiance deposited directly upon a cislunar object, solar radiance is deposited upon celestial bodies such as the Earth or Moon and subsequently reflected off of other objects. This is termed the albedo effect, and is quantified as a percentage of reflected light (Coakley, 2003). For the Earth and Moon, the average albedo effect is approximately 0.3 (NASA, 2019) and 0.1 (NASA, 2017)

respectively. Note that while these signal contributing terms are acknowledged here, they have not been implemented in this research.

Reflection Loss. Once the light reflects from the object, there is an additional loss term, which is captured by the multiplication of the Lambertion reflection coefficient, ψ, and the power that falls upon the surface of the object (Vallerie, 1963). For a spherical object, the power term is the muliplicative of the solar irradiance and a geometric term

$$P = I\pi r_{serv}^2 \tag{34}$$

For a sphere with surface reflectance C_D, the equation below captures the variation of ψ, over solar phase angle, β. This term is a multiplicative loss with respect to the incoming light. The solar phase angle is defined as the angle between the Sun, the object, and the observer

$$\psi = \frac{2C_D}{3\pi^2}(sin(\beta) + (\pi - \beta)\, cos(\beta)) \tag{35}$$

The reflected power from each source (i.e., direct and albedo) is additive which results in a total reflected power of

$$P_{reflected} = \sum_{i=1}^{numsources} P_i \psi_i \tag{36}$$

Path and Atmospheric Losses. The power received by the observer, if treated as originating from a point source, can be calculated as a simple path loss which represents the spreading of the solar light over the distance, R, from the object to the observer.

For observers on the Earth's surface, there is an additional loss due to refraction through the Earth's atmosphere. Below $20°$ elevation, these losses become deleteriously large, and ground-based telescopes do not typically operate below this threshold. The inverse of this loss term is called atmospheric transmittance, τ_{atm}, and is calculated with a tool such as the AFIT Laser Environmental Effects Definition and Reference (LEEDR) (Stern and Wachtel, 2017). For space-based telescopes, τ_{atm} is equal to one because there are no atmospheric losses in space. Therefore, the received by the observer aperture is

$$P_{in} = \frac{P_{reflected}}{R^2}\tau_{atm} \tag{37}$$

Optical Gain. At this point, the signal has reached the outermost edge of the observer's sensing chain, the telescope. There is simultaneously a signal gain and signal loss effect of the telescope and its associated optics. The inverse of the signal loss is called optical transmittance, τ_{opt}, which is due to imperfections and other losses due to the optics; usually a system design parameter, a typical value for this term is 0.9 (Stern and Wachtel, 2017). The optical gain is due to the shapes of mirrors and lenses, and is calculated as the square of the telescope aperture diameter. Therefore, the power on the detector may be calculated by

$$P_{Detector} = P_{in}\tau_{opt}\pi A_{RCVR}^2 \tag{38}$$

where A_{RCVR} is the aperture diameter in meters.

Upon hitting the detector, the photons from the signal are converted to discretized electrons, denoted by N_e. This term is a function of the power on the detector, $P_{Detector}$, detector efficiency,η, integration time, t_{int}, and average wavelength detected,λ_{avg}. The

following equation calculates this term, where h and c are Planck's constant and the speed of light respectively.

$$N_e = \frac{P_{Detector} \cdot \eta \cdot \lambda_{avg}}{hc} t_{int} \tag{39}$$

There are two primary forms of noise associated with this process: Dark noise (N_D) and read noise (N_r). Both of these terms are properties of sensors, with typical values of 12 electrons per pixel per second and 6 electrons per pixel respectively (Stern and Wachtel, 2017). Based upon the system specifications outlined in Stern and Wachtel (2017) as well as Ackerman, et al. (2015), it is safe to assume that a typical satellite will fall within the instantaneous field of view (IFOV) of a single pixel for both ground and space-based systems. This is useful, because the SNR equation below is dependent upon, n_{pixel}, which is the number of pixels that the signal of interest illuminates.

In addition, for ground-based telescopes there is a noise term for sky brightness due to moonlight scattering through the Earth's atmosphere as described by Krisciunas and Schaefer (1991). For this research, these effects will be ignored with the exception of viewing angles that are close to the Moon, for which an exclusion zone may be applied due to significantly increased scattering.

$$SNR = \frac{N_e}{\sqrt{N_e + \eta(N_d) n_{pixel} + N_r^2}} \tag{40}$$

Using the above terms, the signal to noise ratio (SNR) can be calculated. This term will be critical to the evaluation of SDA architectures, as will be seen in future sections.

2.3.2. Impacts of Solar Geometry and the Synodic Period

Over the passage of time, the geometry of the Sun, Earth, and Moon with respect to the object and observer create exclusion zones for the electro-optic SDA sensors. The first category of exclusion zones is due to saturation of the sensor due to the brightness of the Sun and the Moon. This results in an exclusion zone from the boresight of the sensor typically on the order of $40°$ for the Sun, $10°$ for the moon from Earth-based sensors, and $5°$ for the Moon from space-based sensors (Stern and Wachtel, 2017). Albedo effect-based Earth exclusion zones are feasible, due to Sun light reflecting from the Earth's surface into an observer sensor, but they were not considered for this research.

Additionally, the Earth and Moon can both block light from reaching the object of interest, resulting in an inability of the observer to detect it. This creates an effective exclusion zone. These effects are dependent upon the distance from the shadowing body, and are automatically calculated by STK.

The Moon-Earth-Sun geometries change over the course of time, exhibiting periodic behavior over a Lunar synodic month, which is 29.5 days long. This is in contrast to the Lunar sidereal month of 27.3 days, which is the time it takes for the Moon to rotate around the Earth with respect to a fixed star field (Lucey). The Earth, Sun, and Moon have matching relative positions in the synodic plane at the beginning and end of this period. However, the lunar orbital plane is inclined with respect to the ecliptic plane by 5.145° (NASA, 2017). Without accounting for precession, it would take one year to observe all possible relative geometries. Because the lighting conditions in a scenario can vary significantly depending upon these geometries, it is important that these initial conditions be accounted for in the cislunar SDA model.

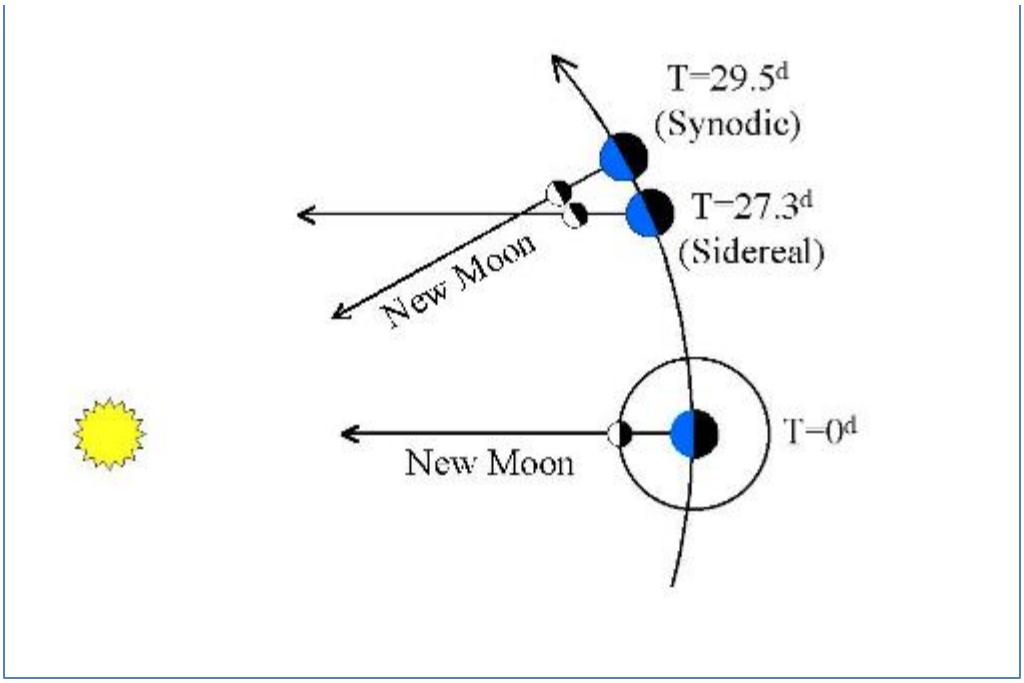

Figure 6: Synodic vs. Sidereal Periods (adapted from Lucey)

2.4 MBSE for SDA Systems

Similar work has already been performed by Stern and Wachtel (2017) for an MBSE approach for optimization of GEO SDA architectures using Genetic Algorithms and parallel computing. This research is an initial foray into applying an analogous MBSE framework for cislunar SDA. To date, no tools have been developed explicitly for analysis of electro-optic cislunar SDA architectures.

2.4.1. Evaluation of SDA Architectures

According to JP 3-14 (US JCS, 2018) the Detect and Track functions of SDA are of utmost importance, and are the primary physics-based metrics for SDA systems. This is consistent with the assertions of Stern and Wachtel (2017), as well as Felten (2018), each

of whom developed evaluation frameworks for SDA of the geosynchronous orbit. Also of primacy to Government decision makers is the cost associated with these architectures.

The utility of an evaluation framework is in comparing architectures. To do so requires qualitative or quantitative metrics produced by the simulation. This is typically performed by using a top-level metric that incorporates lower level metrics. One simplistic way of doing this is with a weighted sum objective function (Collette & Siarry, 2003)

$$f_{obj}(X) = \sum_{i=1}^{k} w_i f_i(X) \tag{41}$$

where $f_i(X)$ are objective functions and w_i is the weight of each function, with

$$\sum_{i=1}^{k} w_i = 1 \tag{42}$$

For this application, the lower-level metric functions should represent (1) the ability of the architecture to detect the object, (2) the ability of the architecture to track the object, and (3) the cost of the architecture (Stern and Wachtel, 2017).

Detect. Detector Signal to Noise Ratio (SNR) may be used as a proxy for detection of an object. If the SNR is above a threshold value, then a successful detection is assumed. The sources vary in the minimum value required for detection, but both Stern and Wachtel (2017) and Felten (2018) conservatively opt for an SNR of six, the highest threshold in the literature.

These SNR values must be manipulated to form a useful metric representing some detection-based parameter of interest. The mean detectable object size (MDOS) is a suitable metric for a scenario with 10's to 100's of objects of varying sizes to track (Stern and Wachtel, 2017).

$$MDOS = \frac{\sum_{i=1}^{n_{objects}} \left(\frac{\sum_{j=1}^{n_{obs}} size_j}{n_{obs}} \right)_i}{n_{objects}} \tag{43}$$

where $n_{objects}$ is the total number of objects, n_{obs} is the number of observations of the i^{th} object, and $size_j$ is the size of the i^{th} object observed in its j^{th} observation.

It would not, however, be appropriate for a cislunar scenario with only one object of interest with a fixed size; this will be explored further in Chapter III: Methodology.

Track. For traditional near-earth SDA, a successful object "track" means that a successful Orbit Determination (OD) has been performed. Optical SDA systems produce two angles per measurement; the classical technique for performing OD with these measurements, developed by Gauss, leverages formulae from the two-body problem and assumes that satellite motion is restricted to a single plane (Bate, et al., 1971). These are flawed assumptions for the three-body problem. While there is some research into OD for cislunar orbits, they focus on cooperative tracking techniques (Woodward, et al., 2011) as opposed to optical tracking.

In general, the quantity of measurements plays a large role in the accuracy of an OD (Woodward, et al., 2011). In addition, the accuracy of the estimate decreases as the time from the measurement decreases (Wiesel, 2010), which is amplified for cislunar orbits due to orbital instability. This allows for a general parameter based upon the number of tracks over a given time period as well as the time between tracks to represent the "goodness" of an SDA architecture without selecting and applying a particular algorithm.

Stern and Wachtel (2017) performed an analogous generalization for a track metric, utilizing the Mean of Max Observation Time Gap (MMOTG) to account for the maximum time between object tracks.

$$MMOTG = \frac{\sum_{i=1}^{n_{objects}} \left[\max_{1 \le j \le n_{obs}} \left(t_1 - t_{start}, t_{j+1} - t_o, t_{end} - t_{n_{obs}} \right) \right]_i}{n_{objects}} \quad (44)$$

where $n_{objects}$ is the total number of objects, n_{obs} is the number of observations of the i^{th} object, and t_j is the time of the j^{th} observation of the i^{th} object, with t_{start} and t_{end} representing the scenario start and end times respectively.

Cost. While it is critical that SDA systems be able to detect and track an object to meet their technical requirements, they will not be built if they are unaffordable. To this end, Stern and Wachtel (2017) developed a series of parametric cost estimation formulas.

The first two equations are for procurement and annual acquisition cost of ground-based telescopes. The former was developed by regression analysis for the Visible and Infrared Survey Telescope for Astronomy (VISTA) using a power equation found in the literature, and a multiplier of two to account for military-unique requirements. The annual operating cost of ground-based telescopes is often found to a percentage of the procurement cost. Stern and Wachtel used 0.20 as a midpoint of multipliers across the literature.

$$C_{Tel} = (\$4{,}000{,}000)A^{2.45} \quad (45)$$

$$C_{TelOp} = (0.2)C_{Tel} \quad (46)$$

where A is the telescope aperture diameter in meters.

The second set of equations are for satellite procurement and operation. Stern and Wachtel derived the linear procurement equation from the work performed by Stahl, Stephens, Henrichs, Smart, and Prince (2011). The operating cost equation was derived by calculating the number of personnel required to operate a constellation by the average cost of such a staff, which yields a per-constellation cost of $400,000,000.

$$C_{Sat} = (\$400{,}000{,}000)A \tag{47}$$

$$C_{SatOp} = (\$9{,}900{,}000)n_{constellations} \tag{48}$$

where A is the telescope aperture diameter in meters and $n_{constellations}$ is the number of satellite orbit types (e.g., LEO, GEO, polar GEO).

2.5 Summary

The MBSE approach to evaluating cislunar SDA architectures leverages each subject reviewed in this chapter. The CR3BP cislunar dynamics reveals the requirement for numerical methods in evaluating cislunar SDA architectures. The signal chain of electro-optic SDA systems shows several factors that dynamically contribute to SNR and thus detection and tracking performance: range, solar phase angle, and solar/lunar exclusion angles. The lack of existing research into cislunar SDA and corresponding architecture evaluation methods led to comparisons with GEO SDA systems, and the foundational work by Stern and Wachtel; their detect and track metrics are not, however, adequate for cislunar SDA and must be adapted.

III. Methodology

3.1 Chapter Overview

This research leverages STK and MATLAB for modeling and simulation. First, STK will be used to calculate the cislunar transfer orbit for the on-orbit object. Then, for each of the SDA architectures, STK will be used to determine access times and position vectors, as constrained by earth occlusion and sensor exclusion criteria such as Sun and Moon angles. This information will feed a MATLAB-based model to calculate individual SDA sensor "fitness" parameters such as ability to detect and track the servicing satellite. This data will be used to calculate an overall architecture "fitness" based upon overall ability to detect and track the transiting satellite, as well as an estimated financial burden for fielding and operating the systems.

3.2 Problem Description

3.2.1. Cislunar Reference Scenario

Testing the evaluation framework for cislunar SDA requires a cislunar reference scenario. In this scenario, an *object* of interest is in an L1 Lyapunov orbit. This could be a satellite, or it could be space debris. The object orbits continually for one orbit. The individual SDA systems, which will be termed *observers*, will attempt to detect and track the object over the entire scenario.

3.3 The Cislunar SDA Model

Similar work has already been performed by Stern and Wachtel (2017) for an MBSE approach for optimization of GEO SDA architectures using Genetic Algorithms

and parallel computing. This research is an initial foray into applying an analogous MBSE framework for cislunar SDA. The elements of their work which will not be mirrored at this point are the genetic optimization algorithms and the application of parallel computing. Their research leveraged AGI's STK® for orbit propagation and access calculations, and Python for management scripts and other calculations. This model utilizes AGI's STK® as well as ASTROGATOR ® for orbit propagation and access calculations and MATLAB for management scripts and other calculations.

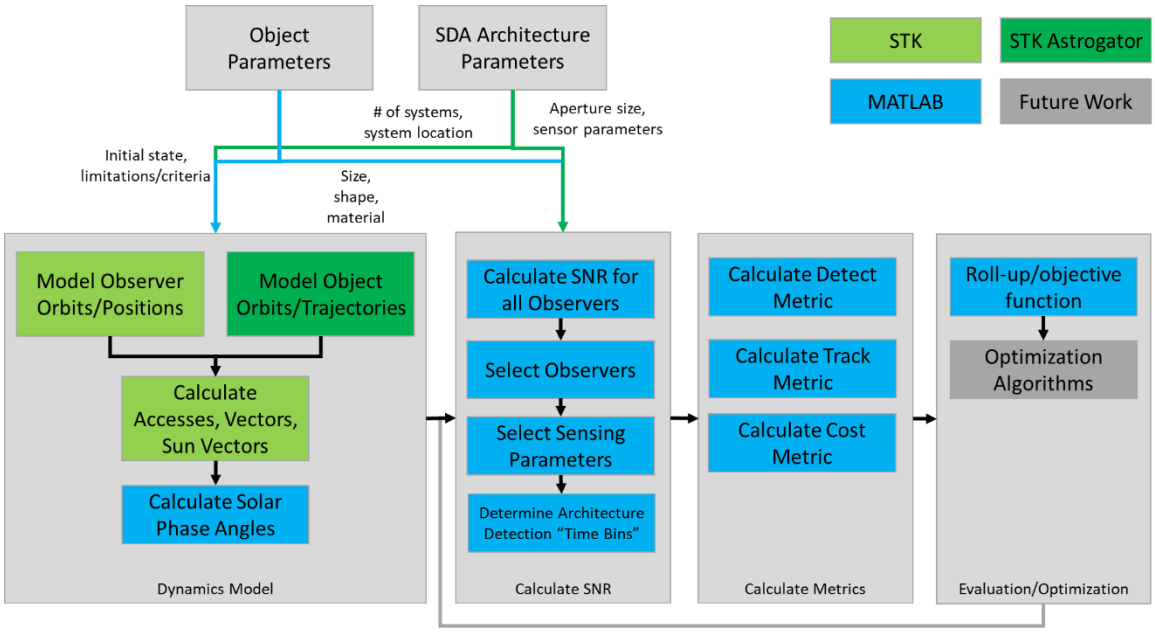

Figure 7: Data Flow Diagram

The functions of the cislunar SDA model are depicted in Figure 7. The initial inputs to the model are a set of parameters for the object and SDA architecture parameters. AGI's STK® and Astrogator® will be used to create the cislunar orbit and corresponding transfer

orbit for the object. Then, for each of the possible observers, STK® will be used to determine the position of the objects in time, as well as sensor exclusion criteria. This information will feed a MATLAB®-based model to calculate solar phase angles, calculate individual observer SNR. This data will be used to calculate an overall architecture "fitness" based upon overall ability to detect and track the object, as well as an estimated financial burden for fielding and operating the systems.

3.3.1. Dynamics Model

The initial condition information feeds a dynamics model, the goal of which is to calculate the geometry-based variables for observer SNR calculations.

Creating Object Orbits. Within this block, MATLAB is used in concert with STK's Astrogator tool to instantiate the object in its L_1 Lyapunov orbit. The linear first-order approximation to the CR3BP from section 2.2.3 is implemented in MATLAB to determine estimated initial conditions for the object along the x-axis. An Astrogator control segment is generated to implement the differential corrector described in section 2.2.5 which controls the velocity in the y-direction such that object perpendicularly crosses the x-z plane. Astrogator uses a built-in differential corrector (AGI, 2019) that mirrors the single-shooting method used by Parker and Anderson (2013) as well as Grebow (2006).

Model Observer Orbits/Positions. Additionally, STK instantiates the observer locations and/or orbits as applicable, and applies observer limitations such as solar/lunar exclusion angles.

Calculating accesses, position vectors, Sun vectors, and solar phase angles. From there, STK runs the scenario, providing vectors between the object and the sun as well as access-based vectors between the object and the observers. This data is accessed in MATLAB and used to calculate solar phase angles.

The dynamics block passes time-stamped solar phase angles and observer-to-object ranges to the SNR calculation block, which represents the totality of the geometry-based data required to evaluate varying permutations of architectures for the given physical parameters of the SDA architectures; after this point, the remainder of the model is executed with MATLAB.

3.3.2. SNR Calculation

The purpose of this code block is to generate a count of time "bins" over which the selected architecture is capable of successfully detecting and tracking the object. Its inputs are object parameters (size, shape, and material reflectivity) and observer parameters (aperture sizes, architectural element selection, and sensor parameters). This research uses the object parameters in Appendix B: Object Parameters, and observer parameters in Appendix C: SDA Sensor Information.

SNR Calculation. The first step in the process is to calculate the observer SNRs for all possible subsets of observer and aperture size combinations. This is performed using the SNR calculations from Section 2.3.2, using the aforementioned object and observer parameters, solar phase angles, and observer-to-object ranges. Then, all SNR values are compared to the minimum SNR detection threshold to produce a set of binary "time bins" for each observer-object combination that indicate when the observer is able to detect the

object. This provides a pool of detection data from which to determine the ability of the architecture to detect the object over time.

Architecture Selection. Next, the model selects a subset of the observer and aperture size combinations that were pre-determined by the desired architecture.

Tasking and Search. At this point, a tasking algorithm could be used to assign observers to view the object or other objects; this is not implemented in this simplified model because there is only one object to observe. Also at this point, a stochastic search algorithm could be implemented to account for uncertainty in a priori knowledge of object state, or to model searches for objects for which a priori states are unavailable; similarly, this is not implemented in this simplified model and perfect a priori states are assumed. If both tasking and search methods are considered, they would be used to determine which time-phased sets of individual observer detection values will be used to calculate the overall architecture-level detection values in the next step.

Architecture-level Detection. The subset of detection values are compared for each object; if a single observer detects the object for a given "time bin", then the architecture-level detection vector receives a binary flag in that slot. This vector is the output of the SNR Calculation and Tasking block, which is provided to the Calculate Metrics block.

3.3.3. Metric Calculator

The purpose of this code block is to calculate the three evaluation metrics for each architecture: Detection, Track, and Cost. It utilizes the architecture-level detection vector received from the SNR Calculation and Tasking block, as well as the following architecture

meta-data: Observer type **(**GEO, LEO, Ground), number of GEO or LEO constellations, and observer aperture diameter in meters.

Detection Metric. As described in section 2.4.1, Stern and Wachtel (2017) utilized MDOS as a detection metric for determining the mean object (i.e., object) size, from a pool of 10's to 100's of objects of varying sizes, that the architecture could detect. For a cislunar scenario there may be very few objects to observe, and in this research there is only one. Thus, MDOS is not an appropriate detection metric. In this case, it may be more useful to ascertain the percentage of scenario time for which the architecture successfully detects the objects of interest. This term will be called Mean Detect Time, and is calculated by

$$MDT = \frac{\sum_{i=1}^{n_{obj}} \frac{t_{detected,i}}{t_{scenario}}}{n_{obj}} \tag{49}$$

where, $n_{objects}$ is the total number of objects, $t_{detected,i}$is the number of detection time bins for the i^{th} object, and $t_{scenario}$ is the total number of time bins in the scenario.

Track Metric. Stern and Wachtel (2017) performed an analogous generalization for a track metric, utilizing the Mean of Max Observation Time Gap (MMOTG) to account for the mean maximum time between object tracks. Given that there may be extended periods without an object track for the cislunar scenario, using the MMOTG may not be the most useful track metric as it would be biased towards long track gaps.

Instead, this research will utilizes the Mean Track Time (MTT) and Mean Time Between Tracks (MTBT), which represent the average time of each track and the average time between tracks respectively. They are defined as follows:

$$MTT = \frac{\sum_{i=1}^{n_{obj}} \frac{\sum_{j=1}^{n_{obs,i}} T_{obs,j,i}}{n_{obs,i}}}{n_{obj}} \tag{50}$$

$$MTBT = \frac{\sum_{i=1}^{n_{obj}} \frac{\sum_{j=1}^{n_{gaps,i}} T_{gaps,j,i}}{n_{gaps,i}}}{n_{obj}} \tag{51}$$

where n_{obj} is the total number of objects to be tracked (i.e., objects) in the scenario, $n_{obs,i}$ is the number of observations for the i^{th} object, $T_{obs,j,i}$ is the time period of the j^{th} observation of the i^{th} object, $n_{gaps,i}$ is the number of observation gaps for the i^{th} object, $T_{gaps,j,i}$ is the time period of the j^{th} observation gap of the i^{th} object. Smaller MTBT is desirable, as it indicates more frequent observations. In contrast, larger MTT is desired as it indicates a longer custody period.

Cost Metric. This metric leverages the cost equations presented by Stern and Wachtel (2017), which can be found in Section 2.4.1. This metric does not include satellite launch cost as there are numerous launch and employment methodologies available now: From the 60 Starlink satellites launched in a single Falcon 9 rocket (Adams, 2020) to hosted payload acquisitions to be demonstrated by the Air Force on the Japanese QZSS satellite (McLeary and Hitchens, 2019). This makes the cost metric a bounding case for this research.

3.3.4. Architecture Evaluation

The purpose of this code block is to create the roll-up metric for each architecture, based upon the Detect, Track, and Cost metrics received from the Calculate Metrics code

block. This is also where an optimization algorithm would be implemented; this is, however, outside the scope of this research.

Roll-up Metric. This research will use the weighted sum objective function described in section 2.4.1:

$$f_{obj}(X) = \sum_{i=1}^{3} w_i f_i(X), \text{ where } \sum_{i=1}^{3} w_i = 1 \quad (52)$$

For this case, $i = 1,2,3$ describe the detect, track and cost metrics with equal weights of 1/3. For the track metric, there are actually two sub-metrics (MTT and MTBT) which will have equal weights of 1/2 within the track metric.

Establishing "baseline" for Cislunar SDA. It would be useful to compare each architecture to a baseline architecture. For this research the optimal GEO SDA architecture identified in Stern and Wachtel (2017) will be the baseline. This is because no baseline architecture for cislunar SDA exists, and also because it is useful to illuminate the differences between requirements for GEO and cislunar SDA. This architecture is defined (with modifications) below:

- Three 1-meter telescopes at La Palma, Canary Islands
- Three 1-meter telescopes at Mauna Kea
- Four 1-meter telescopes at the Indian Astronomical Observatory
- Four satellites in 1000 km equatorial LEO orbits with 30 cm aperture sensors
- Four satellites in GEO with 30 cm aperture sensors
    - This was changed from three satellites in GEO with 45 cm aperture sensors to simplify modeling and analysis

Prior to calculating the roll-up architecture metric, each individual metric will be normalized to the corresponding metric value for the Stern and Wachtel architecture. This

will leave the Stern and Wachtel architecture with a roll-up value of unity. Better architectures will have a value less than unity, and worse architectures will have a value greater than unity.

3.4 Test Cases

To support this research there are two types of test cases: Those that provide results of the architectural analyses, and those that provide context for interpreting them. The next section introduces the latter type of test case.

3.4.1. Analyzing Geometric Effects Across the Synodic Period

This test case is designed to enable understanding of the relationship between the synodic period and SNR for the scenario. In the nominal scenario, the objects provide dynamic ranges with respect to the observers over the course of their Lyapunov orbits. The case described here provides understanding as to bounding cases for the scenario, decoupled from the dynamics of the Lyapunov orbit. The intent of this test case is to understand the impacts of solar phase angles, solar exclusion angles, and lunar exclusion angles as a function of Synodic period.

Four objects are placed at lunar orbital radius in the synodic plane, spaced 90 degrees with the respect to the earth. Four objects are selected in lieu of running the model four times, which saves time during the multi-hour runs on a home computer. These objects are propagated using the STK two-body propagator, ignoring the effects of lunar gravity. This test case utilizes all available observers with the parameters described in Appendix C: SDA Sensor Information. This particular test case is repeated both with and without solar and lunar exclusion angles. All four objects are modeled within one test case to simplify

computational complexity. The test case takes several hours to complete on a personal computer, as it is recording 1 min observation periods of 4 objects for 25 observers over a 29.5 day period, which is more than 4 million data points each with multiple associated data types.

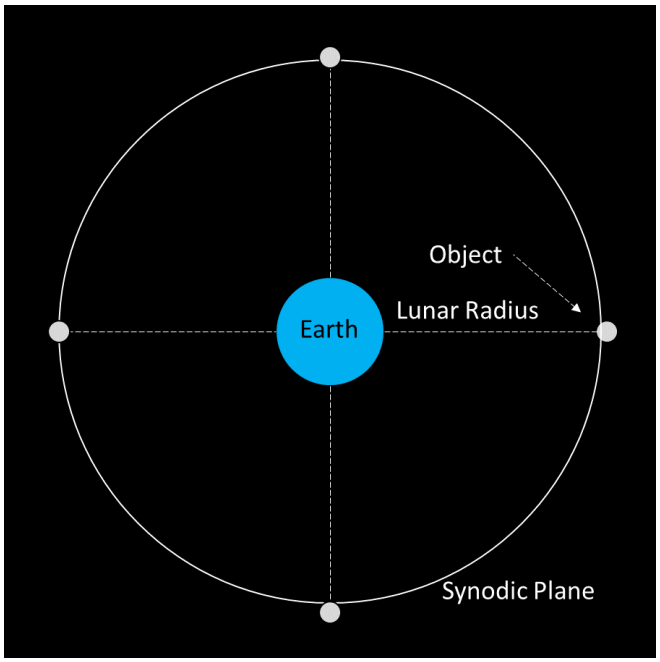

Figure 8: Test Case for Synodic analysis

3.4.2. Evaluating select Cislunar SDA architectures

Initial test runs of the model using all available sensors indicates that for this particular cislunar orbit, the viewing angles from the ground-based electro-optic systems to the object are within the lunar exclusion angle for the entire scenario. Therefore, with the exception of the Stern and Wachtel baseline architecture, ground-based systems will not be included in the test cases for this analysis. The test cases to be analyzed, and their orbital regimes, are listed below in Table 4.

		GEO	LEO	Ground
Reference Comparisons (number of sensors)				
1	Stern & Wachtel (Optimized)	4	4	8
2	GEO and LEO (both polar/equatorial)	4/4	4/4	NA
3	GEO (polar/equatorial)	4/4	NA	NA
4	GEO (polar)	4	NA	NA
5	GEO (equatorial)	4	NA	NA
6	GEO (synodic)	4	NA	NA
7	LEO (polar/equatorial)	NA	4/4	NA
8	LEO (polar)	NA	4	NA
9	LEO (equatorial)	NA	4	NA
10	LEO (synodic)	NA	4	NA

Table 4: Cislunar SDA Test Cases

In addition to the Stern and Wachtel architecture, which consists of 16 sensors and was optimized for GEO SDA, these test cases include a comparison of various combinations of 4-ball GEO and LEO constellations in polar and equatorial orbits, as well as 4-ball GEO and LEO constellations in the synodic plane. The orbital parameters for each constellation is described below in Table 5.

	a (km)	e (deg)	i (deg)	ω (deg)	RAAN (deg)	M
GEO equatorial	42164	0	0	0, 90, 180, 270	0	0
GEO polar			90			
GEO synodic			23		15	
LEO equatorial	1000		0		0	
LEO polar			90			
LEO synodic			23		15	

Table 5: Orbital Elements for SDA Constellations

Each test case will be evaluated at four initial conditions to account for varying solar geometries over the course of the synodic period. Start times were selected such that the Sun-Earth-Moon angle was approximately 0, 90, 180, and 270 degrees. The start times, captured in Table 6, are conveyed pictorially in Figure 9. Each scenario ran for one complete L_1 Lyapunov orbit with parameters $A_{y'} = 15{,}000$ km and $A_{z'} = 20{,}000$km with $\phi = 180°, \psi = 0°$, which is approximately 14 days.

	Date and Time
Scenario 1	14 Sep 2019, 00:00:00
Scenario 2	21 Sep 2019, 12:00:00
Scenario 3	29 Sep 2019, 00:00:00
Scenario 4	6 Oct 2019, 12:00:00

Table 6: Test Scenarios based upon Sun-Earth-Moon Angles

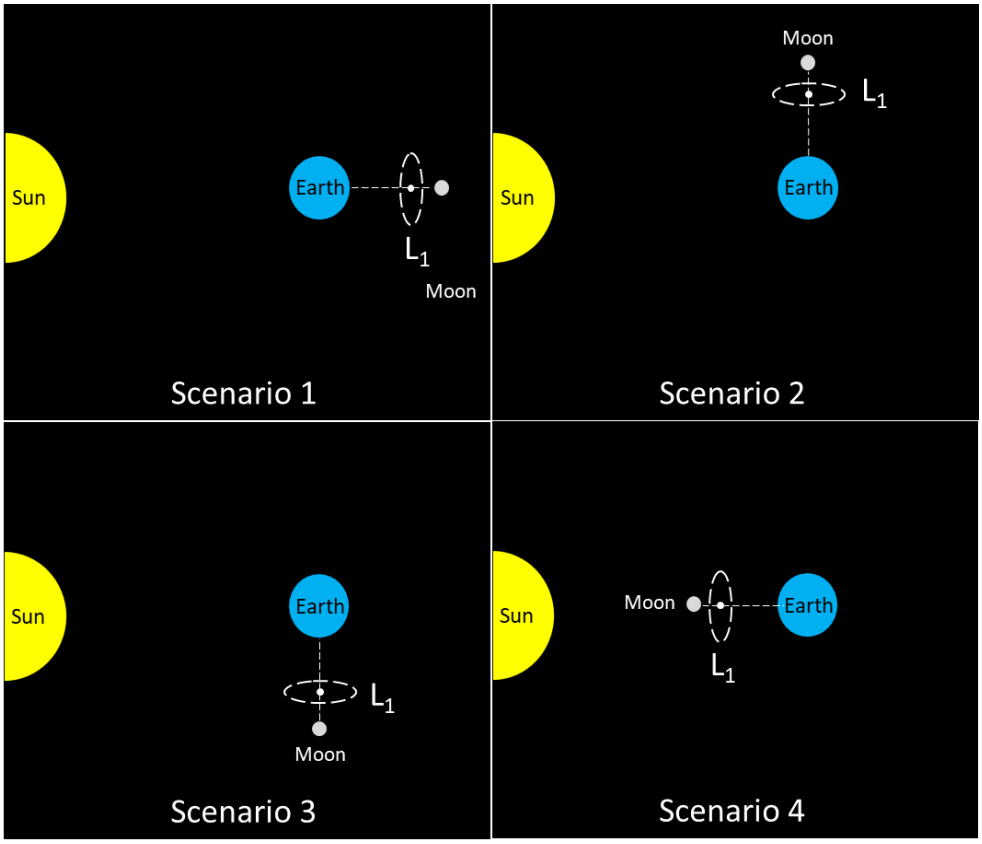

Figure 9: Depiction of Sun-Earth-Moon positions for simulation scenarios

3.5 Summary

This chapter outlined the path forward for model development, data generation, and subsequent analysis. New metrics were developed for assessing the ability of cislunar SDA architectures to detect and track cislunar objects. Finally, test cases were outlined to provide understanding of the cislunar environment on SDA, as well as to provide understanding as to which types of architectures perform the best. While it will evaluate a single reference scenario with multiple initial conditions, the model itself can be used to evaluate other scenarios, making it useful for future research.

IV. Analysis and Results

4.1 Chapter Overview

The primary analysis of this research examines the performance of select SDA architectures. This chapter begins with an analyses of the physics of cislunar SDA to provide context for the subsequent architecture analysis. These physical analyses are performed over the synodic period to provide understanding of dynamics and initial conditions on the scenario. The various test cases are then compared, and an the results are explained.

4.2 Results of Simulation Scenarios

4.2.1. Analyzing Geometric Effects Across the Synodic Period

As depicted in Figures 10 through 13, the SNR for each object drops below the threshold value for approximately four to five days over the course of the synodic period. This behavior is affected overwhelmingly by the solar phase angle, as opposed to range variations, with the latter simply driving oscillations around a period curve. These oscillations are more pronounced for the geosynchronous satellites.

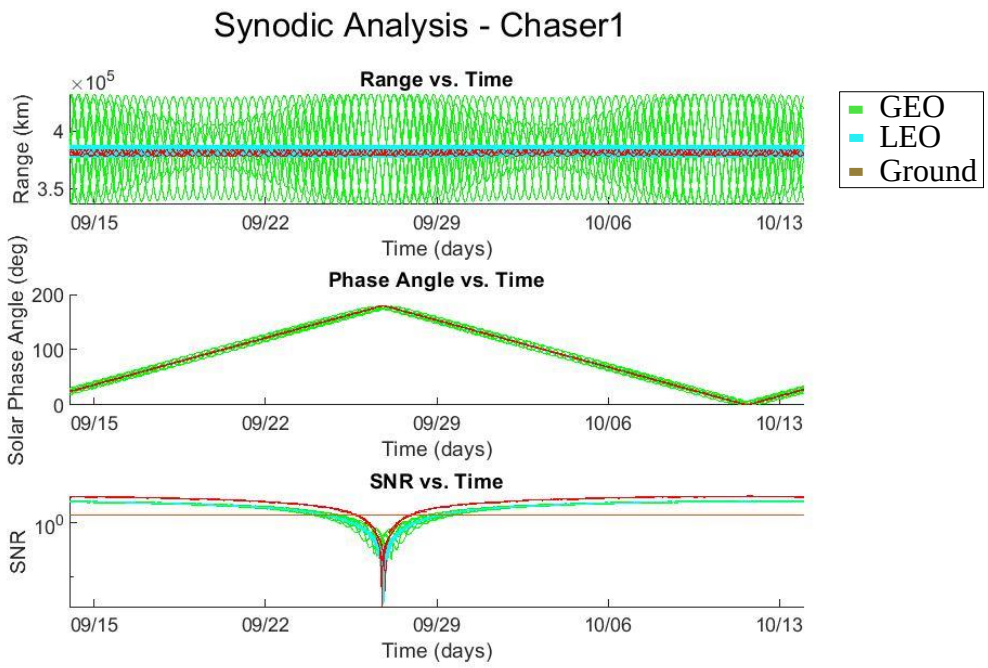

Figure 10: Synodic Analysis for Case 1 without Solar and Lunar Exclusion Angles

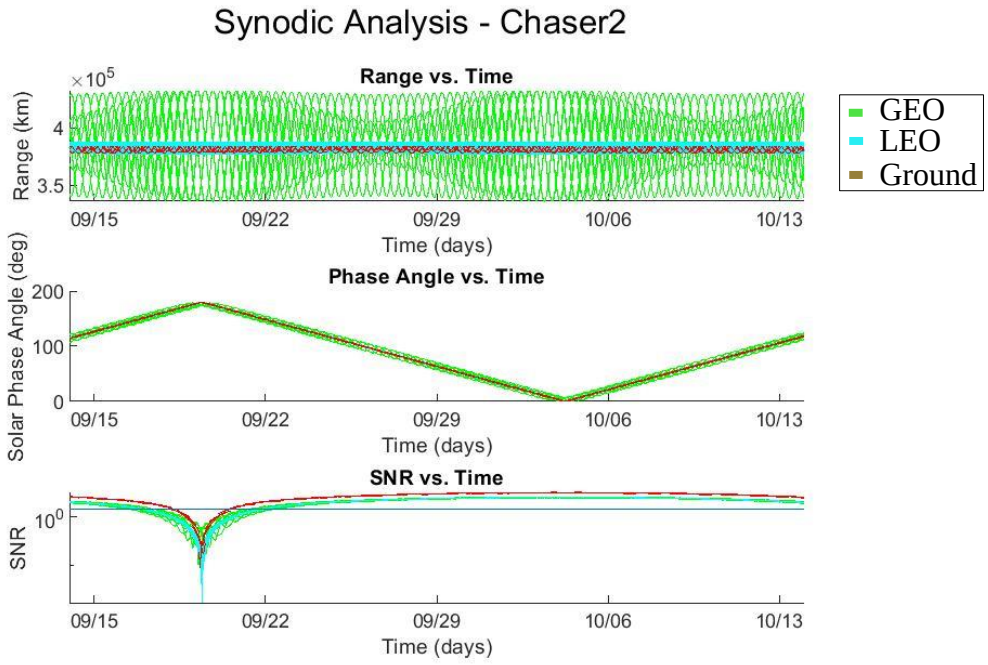

Figure 11: Synodic Analysis for Case 2 without Solar and Lunar Exclusion Angles

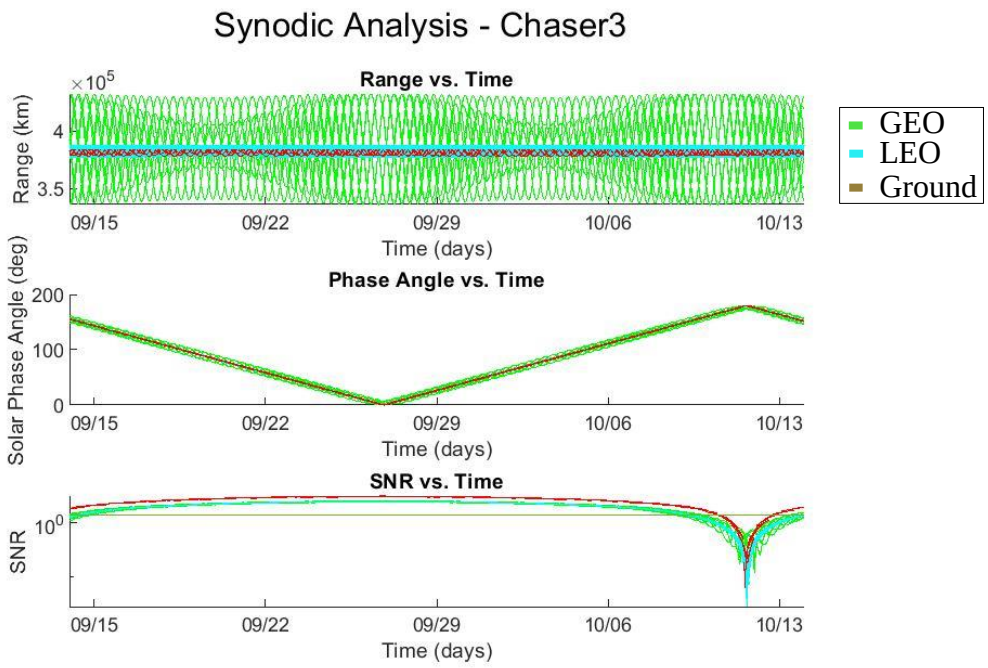

Figure 12: Synodic Analysis for Case 3 without Solar and Lunar Exclusion Angles

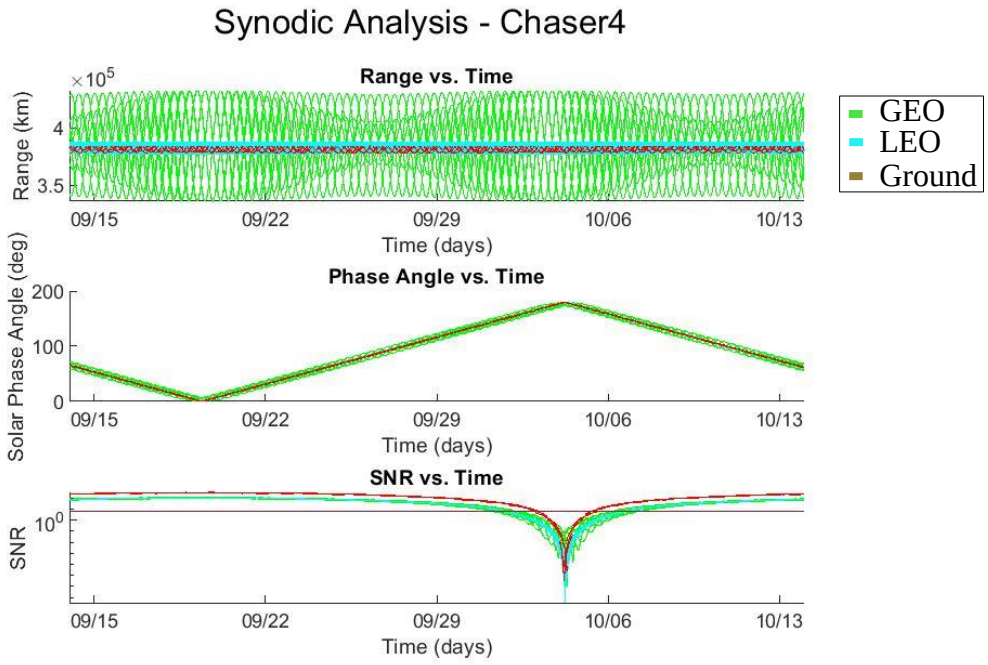

Figure 13: Synodic Analysis for Case 4 without Solar and Lunar Exclusion Angles

When the same scenario is repeated with a solar exclusion angle of 40 degrees and lunar exclusion angle of 5 degrees for space-based observers and 10 degrees for ground-based observers, the SNR minimums are within the solar exclusion angle as captured in Figures 14 through 17. This is because the SNR minimums coincide with maximum phase angles, which take place as the sun approaches the sensor exclusion zone.

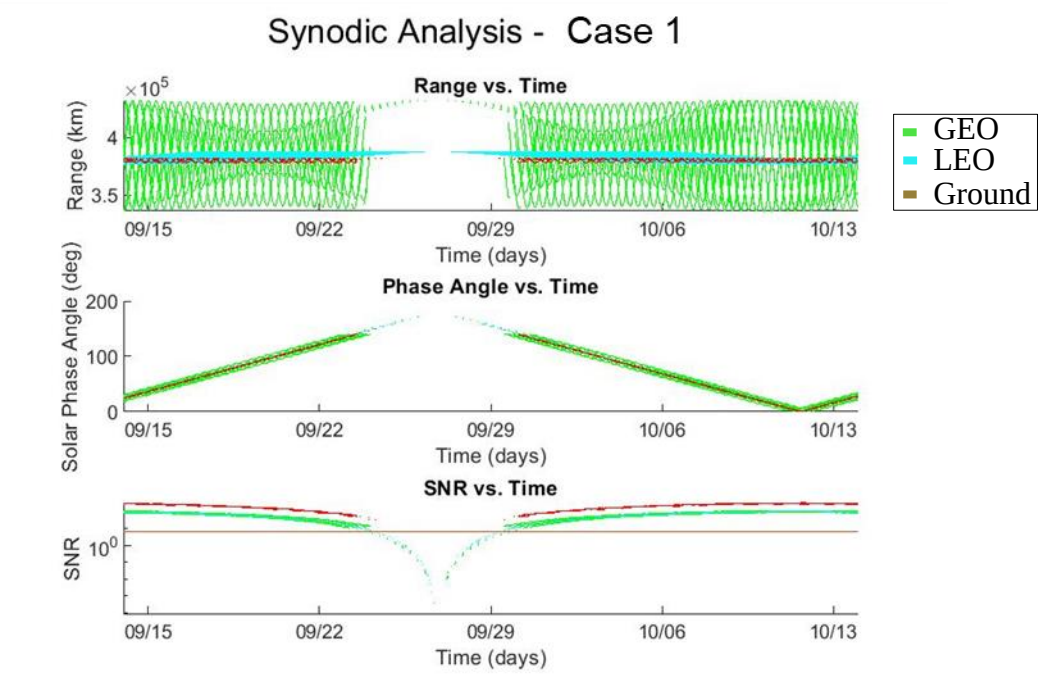

Figure 14: Synodic Analysis for Case 1 with Solar and Lunar Exclusion Angles

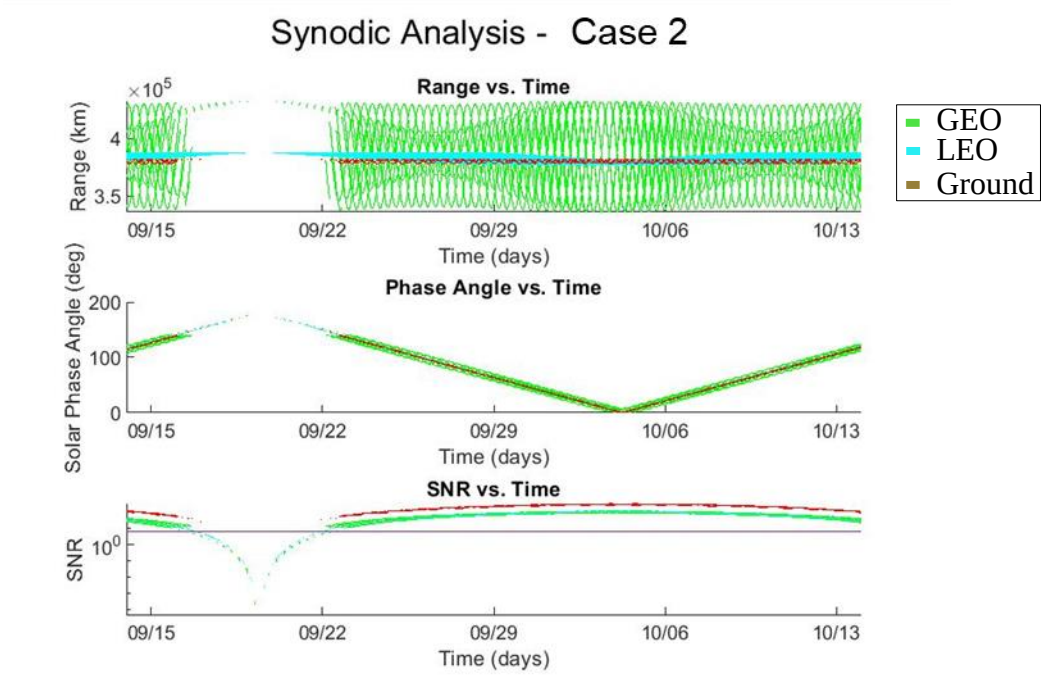

Figure 15: Synodic Analysis for Case 2 with Solar and Lunar Exclusion Angles

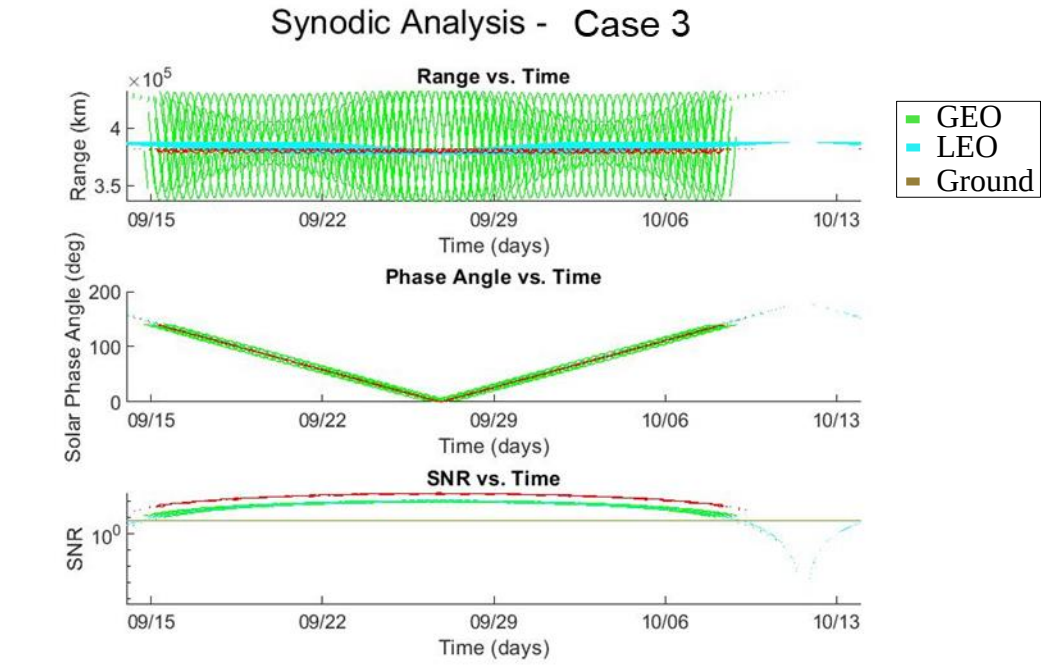

Figure 16: Synodic Analysis for Case 3 with Solar and Lunar Exclusion Angles

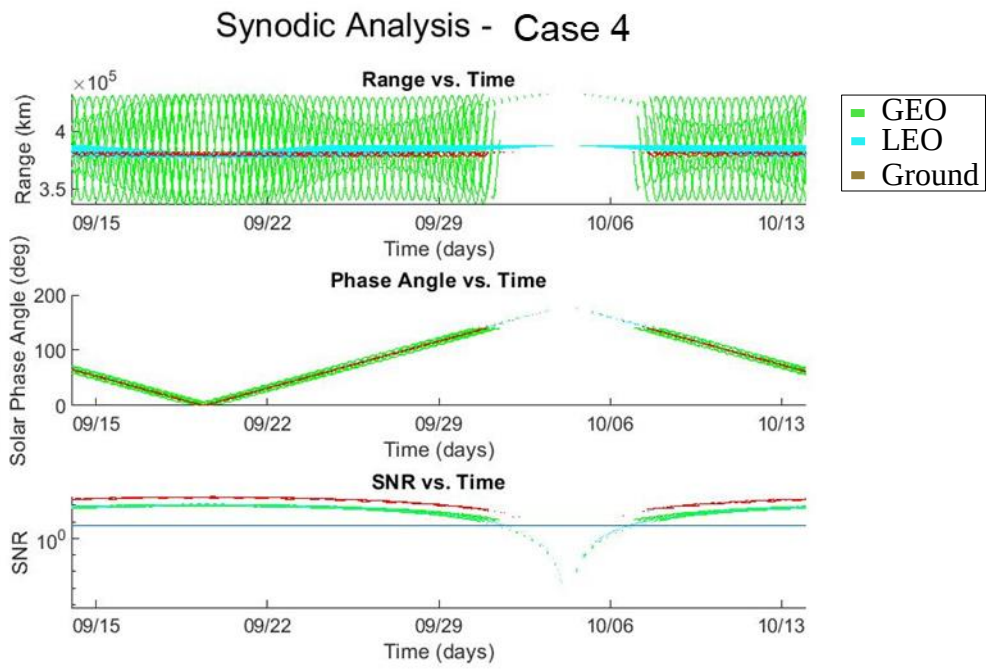

Figure 17: Synodic Analysis for Case 4 with Solar and Lunar Exclusion Angles

In addition to solar exclusion angles and solar phase angles, the cislunar SDA problem is challenged by lunar exclusion zones. Due to the cislunar orbit used in the reference architecture, these may be the dominant challenge for the SDA architectures assessed in this research. As depicted in Figure 18, for the Lyapunov orbit in the reference scenario, the lunar phase angles are within the lunar exclusion zone of 5 degrees for space-based observers and 10 degrees for ground-based observers for the entirety of the scenario for all observers. For each subplot in this figure, all observers within each category (LEO, GEO, Ground) are plotted simultaneously, which makes the LEO plot appear to be a solid line due to the density of the data.

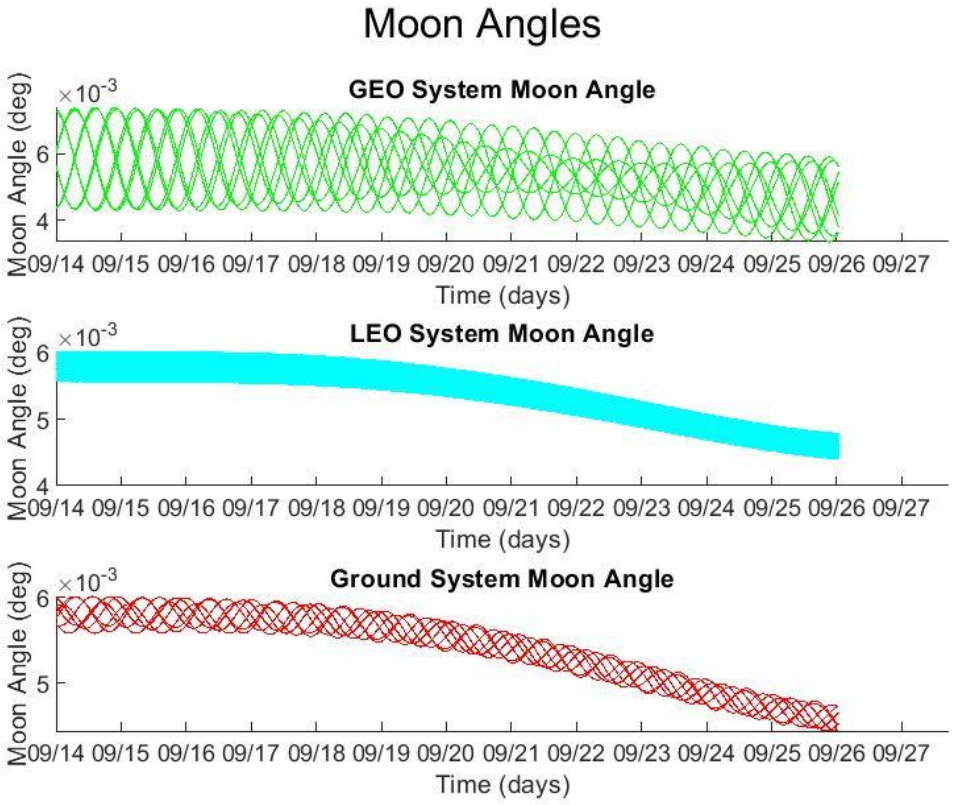

Figure 18: Lunar Exclusion Angles for the Reference Architecure Lyapunov Orbit

All of the above would indicates that a cislunar SDA architecture using traditional orbital regimes and ground-based systems cannot be successful, even if larger optics were used. It would appear to indicate that observers must be placed in non-traditional locations (e.g., high semi-major axis earth orbits, Lagrange points, lunar surface).

4.2.2. Evaluating select Cislunar SDA architectures

While the preceding analysis would indicate that the test cases are incapable of detecting the object due to lunar exclusion zones, executing the model in STK proves otherwise. As depicted in Figure 19, the Earth can block the moon from a satellite observer

field of view without blocking the light reflected from the satellite, providing the observer with short access periods. Not all satellite orbits exhibit this behavior, and not all that do will do so over the course of a synodic period due to variations in relative inclination. This discovery does not, however, improve the performance of ground-based systems as the Earth cannot block the moon from their field of view.

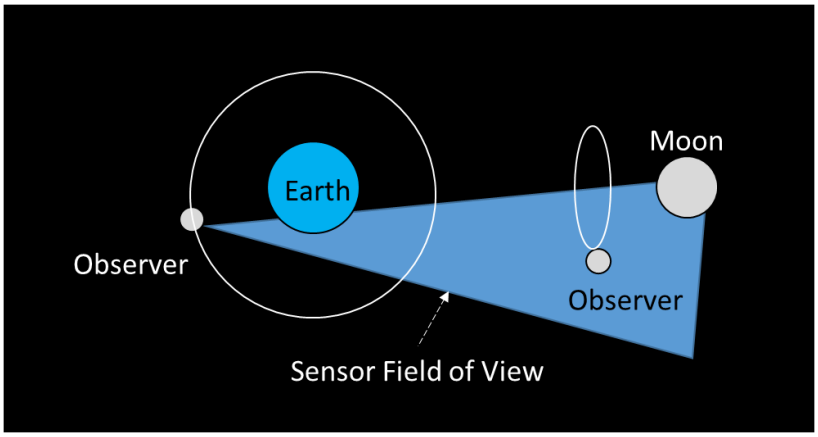

Figure 19: Diagram depicting Earth blocking Moon from Sensor Field of View

The data for the primary test cases is captured in Table 8. Overall, architectures of LEO satellites significantly outperformed GEO architectures and combined LEO/GEO architectures. While the GEO architectures have larger MTTs, their longer orbital periods drive lower MTBTs. The equal weighting of MTT and MTBT, combined with low MDT, drives a poor overall score for GEO-based architectures. Additionally, some GEO architectures do not detect the object at all for the duration of the scenario due to geometry.

		1		2		3		4		5		7		8		9	
		S&W		GEO and LEO		GEO Only		GEO (equ)		GEO (polar)		LEO Only		LEO (equ)		LEO (polar)	
Scenario 1	MDT	7.97%	1.000	7.97%	0.994	0.62%	9.334	0.55%	11.761	0.07%	27.583	12.75%	1.112	7.44%	0.780	5.92%	0.794
	MTT	2.63		2.63		10.25		12.11		4.67		2.90		2.47		2.68	
	MTBT	30.36		30.36		1510.38		1964.90		4936.00		19.79		30.74		42.54	
	Cost ($M)	1990		1952		2192		1096		1096		1712		856		856	
Scenario 2	MDT	3.18%	1.000	3.18%	0.994	0.00%	NA	0.00%	NA	0.00%	NA	3.18%	0.953	3.18%	0.810	0.00%	NA
	MTT	2.51		2.51								2.51		2.51			
	MTBT	75.91		75.91		19758.00		19758.00		19758.00		75.91		75.91		19758.00	
	Cost ($M)	1990		1952		2192		1096		1096		1712		856		856	
Scenario 3	MDT	6.72%	1.000	6.72%	0.994	0.00%	NA	0.00%	NA	0.00%	NA	12.78%	1.256	6.72%	0.810	7.11%	0.877
	MTT	2.53		2.53								3.41		2.53		2.99	
	MTBT	35.10		35.10		19758.00		19758.00		19758.00		23.26		35.10		38.97	
	Cost ($M)	1990		1952		2192		1096		1096		1712		856		856	
Scenario 4	MDT	8.34%	1.000	8.34%	0.994	0.18%	1.757	0.15%	4.061	0.03%	41.287	9.11%	0.987	8.20%	0.805	1.60%	1.127
	MTT	2.44		2.44		3.60		3.75		3.00		2.58		2.42		2.06	
	MTBT	26.83		26.83		1792.91		2192.00		6584.00		25.73		27.07		125.43	
	Cost ($M)	1990		1952		2192		1096		1096		1712		856		856	

Table 7: Test Case Comparison (Blue: <0.9, Green: 0.9 to 1, Yellow: 1-3; Red: >3)

As depicted in Figure 20, while there are GEO observers that meet the line of sight requirements in the scenario, the SNR is below the threshold value due to the solar phase angle.

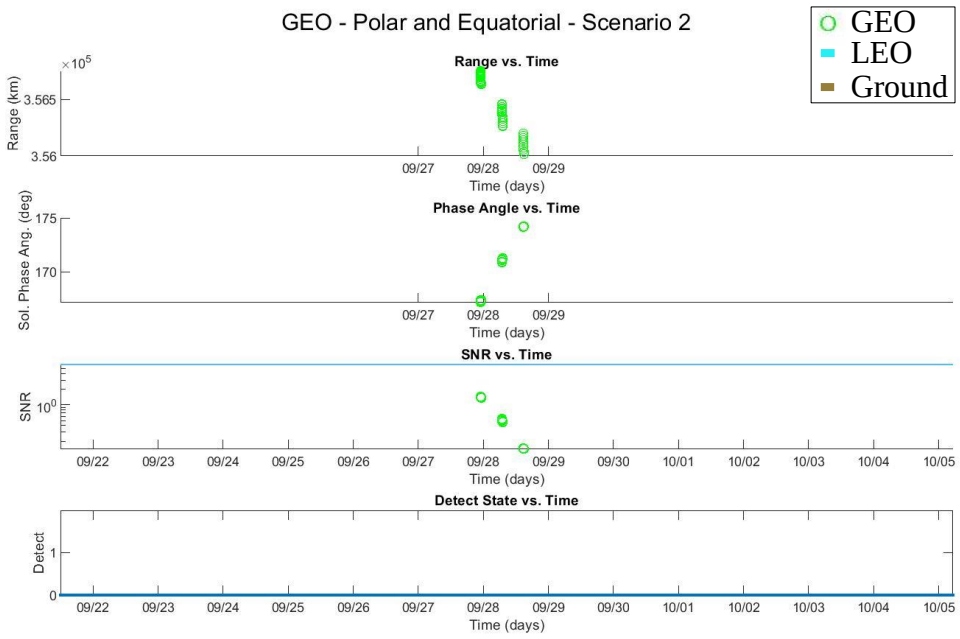

Figure 20: Results for all GEO Constellations in Scenario 2

The LEO-based architectures perform considerably better, with higher MDT and significantly lower MTBT, with only moderately larger MTT. Single plane LEO constellations have similar performance except for Scenarios 2 and 4, where the polar LEO architecture performs markedly worse. As depicted in Figures 21 and 22, this is explained an SNR drop due to solar phase angle maximums. For Scenario 2 in particular, the polar LEO architecture fails to meet SNR criteria during the only period where it meets exclusion criteria and has line of sight to the observer.

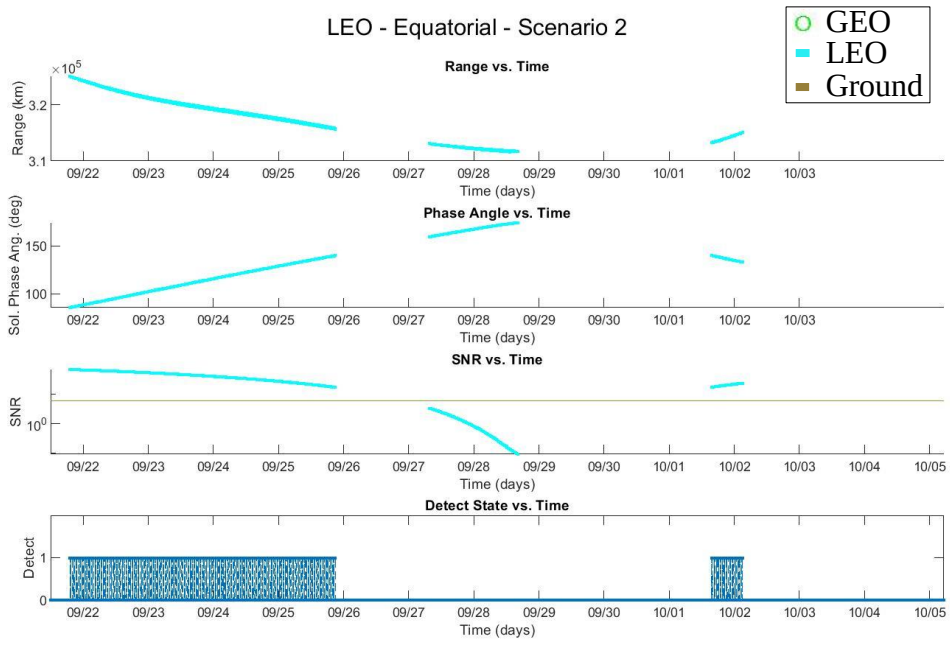

Figure 21: Results for Equatorial LEO Constellation in Scenario 2

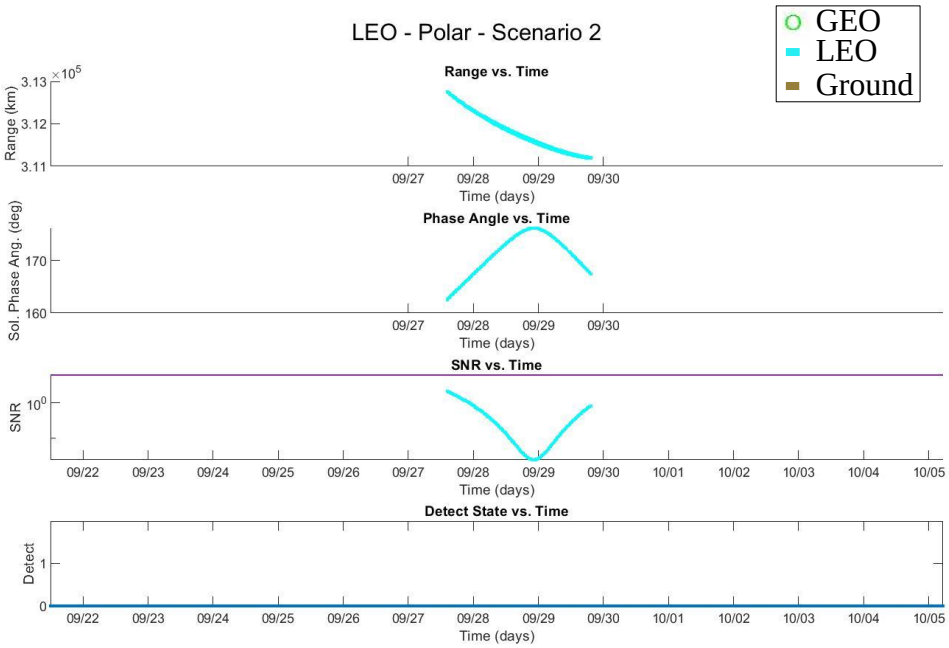

Figure 22: Results for polar LEO Constellations in Scenario 2

It is interesting to note that, while the lunar exclusion angle was a driving factor as predicted, SNR drops due to solar phase angles also played a large role.

4.2.3. Excursion into synodic plane-matched systems

In light of the discovery that the Earth aids in cislunar SDA by blocking the Moon from the observer field of view, systems using synodic plane-matched constellations appear particularly attractive. Geometrically, they should have lower MDTs, higher MTTs, and lower MTBTs. This holds true when compared to equilateral and polar orbits, as shown below.

		3		4		5		6	
		GEO Only		GEO (equ)		GEO (polar)		GEO (synodic)	
Scenario 1	MDT	0.62%	9.334	0.55%	11.761	0.07%	27.583	1.67%	3.913
	MTT	10.25		12.11		4.67		9.68	
	MTBT	1510.38		1964.90		4936.00		555.11	
	Cost ($M)	2192		1096		1096		1096	
Scenario 2	MDT	0.00%	NA	0.00%	NA	0.00%	NA	0.73%	3.815
	MTT							10.29	
	MTBT	19758.00		19758.00		19758.00		1307.60	
	Cost ($M)	2192		1096		1096		1096	
Scenario 3	MDT	0.00%	NA	0.00%	NA	0.00%	NA	1.37%	4.364
	MTT							10.42	
	MTBT	19758.00		19758.00		19758.00		721.74	
	Cost ($M)	2192		1096		1096		1096	
Scenario 4	MDT	0.18%	1.757	0.15%	4.061	0.03%	41.287	1.84%	3.906
	MTT	3.60		3.75		3.00		9.33	
	MTBT	1792.91		2192.00		6584.00		484.85	
	Cost ($M)	2192		1096		1096		1096	

Table 8: GEO Synodic Comparison (Blue: <0.9, Green: 0.9 to 1, Yellow: 1-3; Red: >3)

For GEO architectures, the synodic planes exhibit significant improvement over single constellation architectures for Scenarios 1 and 4. As exhibited in Figures 23 and 24, the geometry of the synodic architecture allows more potential contacts than the polar architecture, resulting in better performance across the board.

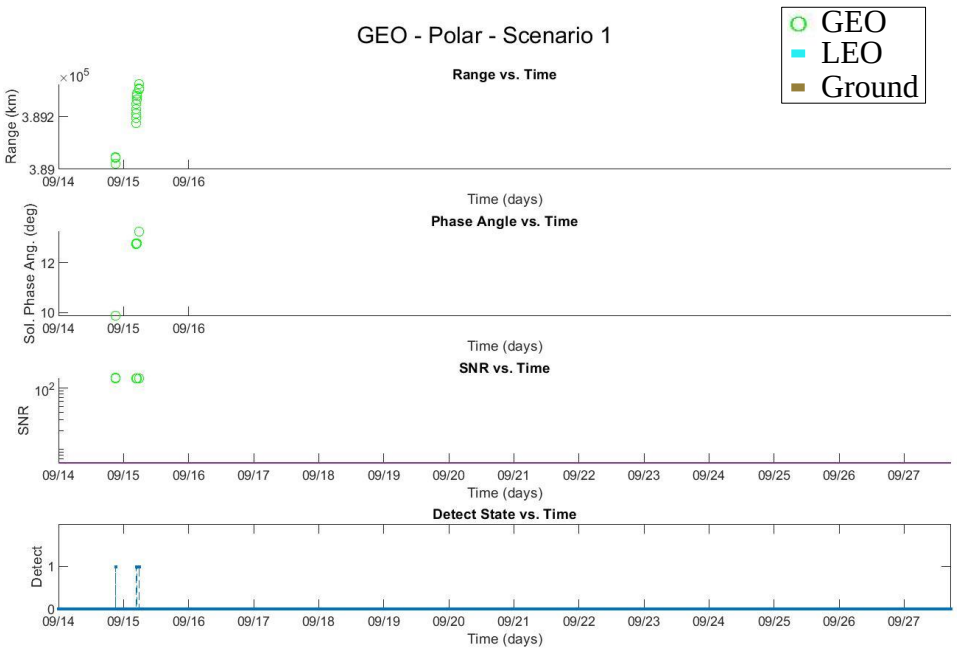

Figure 23: Results for polar GEO Constellations in Scenario 1

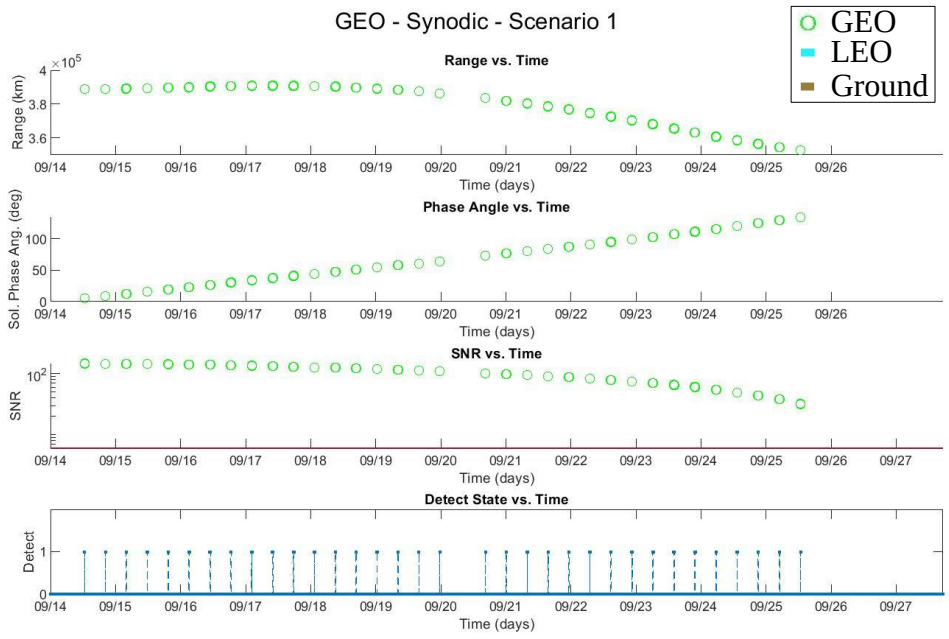

Figure 24: Results for synodic GEO Constellations in Scenario 1

Similarly, the synodic architecture performs better in Scenarios 2 and 3. In Figures 24 and 25, this appears to be due to the fact that the synodic architecture is able to view the object outside of the solar phase angle maximum, where the SNR drops below the threshold value.

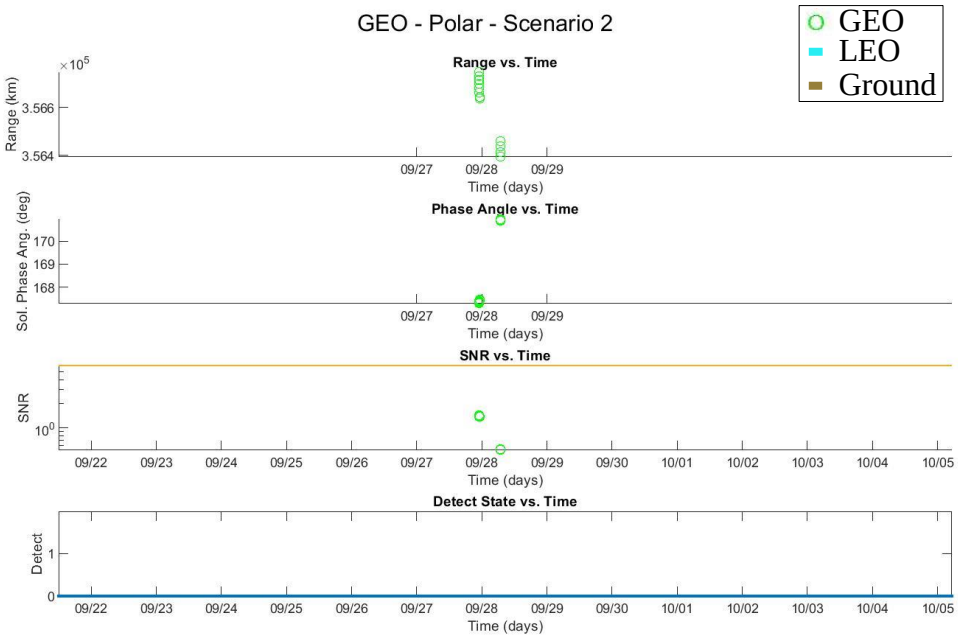

Figure 25: Results for polar GEO Constellations in Scenario 2

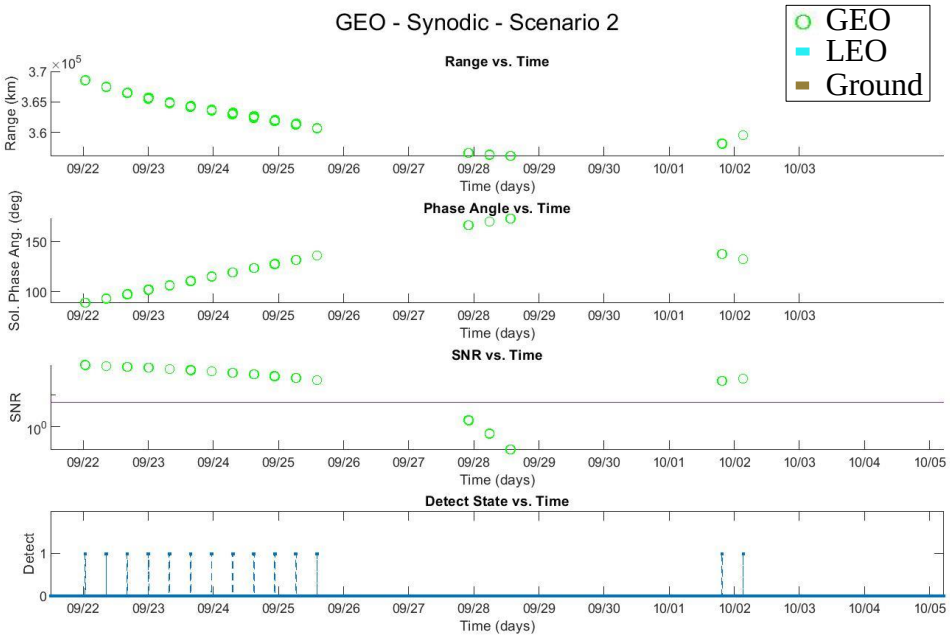

Figure 26: Results for synodic GEO Constellations in Scenario 2

For LEO architectures, the synodic planes exhibit performance very close to the equatorial LEO architecture in all scenarios. The LEO architectures, due to their smaller orbital radius, generally have more opportunities for the Earth to block the moon from their sensor field of view, with the exception of the polar orbit. As evidenced by Figures 27 and 28, the performance differences between the equatorial and synodic architectures are small, due to very similar geometries.

		7		8		9		10	
		LEO Only		LEO (equ)		LEO (polar)		LEO (synodic)	
Scenario 1	MDT	12.75%	1.112	7.44%	0.780	5.92%	0.794	7.48%	0.779
	MTT	2.90		2.47		2.68		2.47	
	MTBT	19.79		30.74		42.54		30.47	
	Cost ($M)	1712		856		856		856	
Scenario 2	MDT	3.18%	0.953	3.18%	0.810	0.00%	NA	3.20%	0.809
	MTT	2.51		2.51				2.49	
	MTBT	75.91		75.91		19758.00		75.00	
	Cost ($M)	1712		856		856		856	
Scenario 3	MDT	12.78%	1.256	6.72%	0.810	7.11%	0.877	6.63%	0.802
	MTT	3.41		2.53		2.99		2.49	
	MTBT	23.26		35.10		38.97		35.07	
	Cost ($M)	1712		856		856		856	
Scenario 4	MDT	9.11%	0.987	8.20%	0.805	1.60%	1.127	8.36%	0.811
	MTT	2.58		2.42		2.06		2.45	
	MTBT	25.73		27.07		125.43		26.83	
	Cost ($M)	1712		856		856		856	

Table 9: LEO Synodic Comparison (Blue: <0.9, Green: 0.9 to 1, Yellow: 1-3; Red: >3)

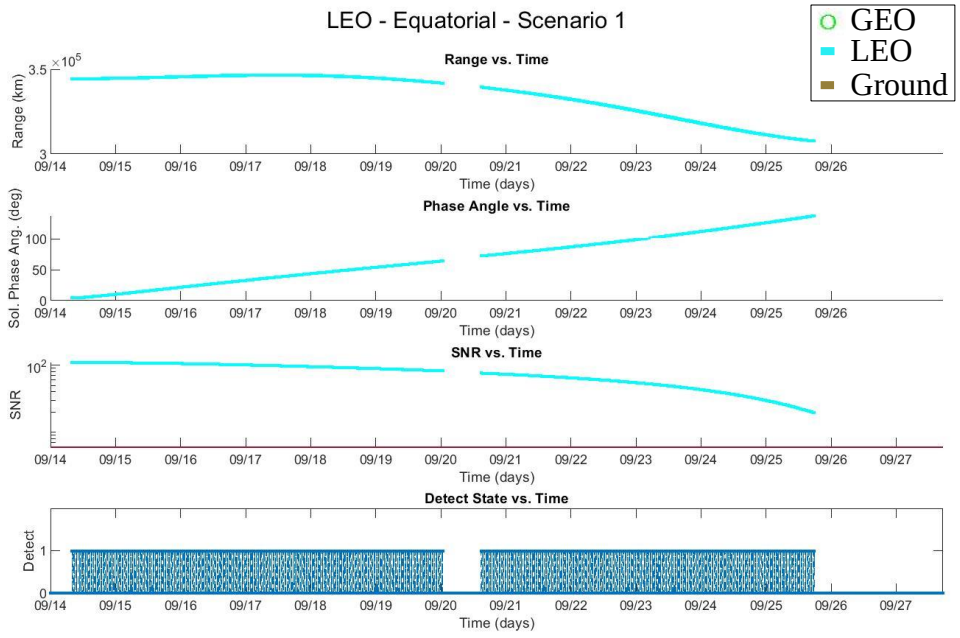

Figure 27: Results for equatorial LEO Constellations in Scenario 1

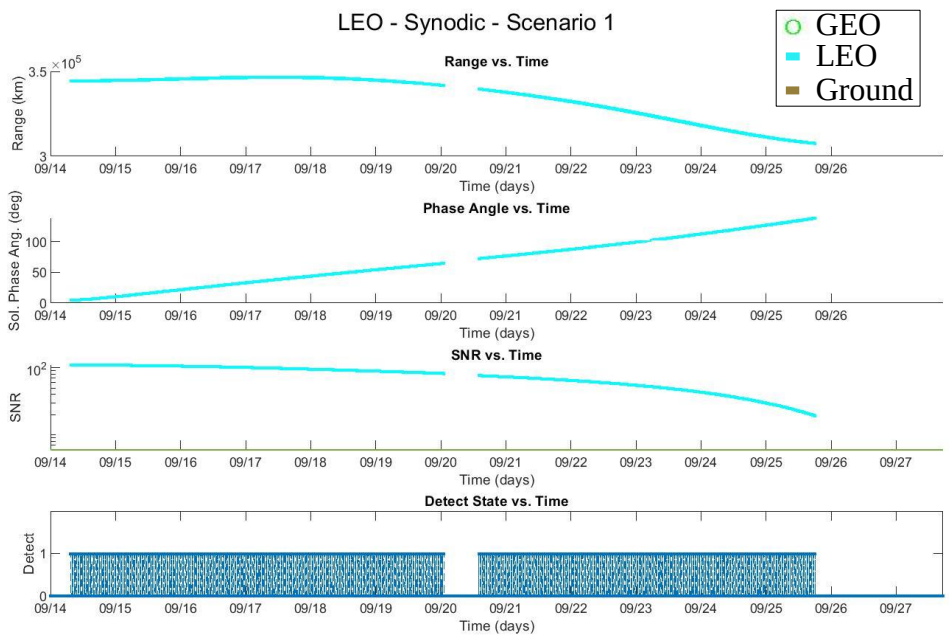

Figure 28: Results for synodic LEO Constellations in Scenario 1

In spite of the physical benefits of the plane-matched systems, there is one potential drawback that requires more research. Typical OD techniques, such as Gauss 'method, require at least two angles from data sources in order for the mathematical theory to work (Bate, et al., 1971). Because the observer and object are plane-matched, this may cause problems for OD techniques. However, for the purposes of this research, the synodic LEO architecture is the best architecture due to its higher overall scores for all scenarios.

4.3 Summary

Analysis of the geometry and physics of cislunar SDA provided insights into limiting factors in architecture performance: Solar phase angle and lunar exclusion angles. Solar exclusion zones were tightly coupled with solar phase angles, which reduced the impact of solar phase angles on SNR. The lunar exclusion angles rendered ground-based sensors

useless, but they were mitigated for space-based observers by the fact that the Earth is able to block the Moon from the sensor field of view for a portion of the orbit when the object is in view. The LEO architectures performed the best overall, and synodic orbits proved to be the best in their orbital category. Overall, the synodic LEO architecture ranked highest.

V. Conclusions and Recommendations

5.1 Chapter Overview

This chapter presents a summary of the gap that this research attempts to fill, a summary of answers to the research questions, and a list of future work.

5.2 Summary of Research Gap

The cislunar space domain is one of growing importance for civil and commercial, and military space organizations. To provide a foundation for space superiority in this domain, the United States must develop systems that are purpose-built for cislunar SDA. Little research has been done with regards to cislunar SDA, and no papers have been published pertaining to Electro-Optic cislunar SDA architectures observing non-cooperative objects. This research is a first step towards exploring this field with the intent that the United States will be better postured to procure and operate optimized cislunar SDA systems.

5.3 Research Questions and Answers

1. ***What are the measures for determining the "fitness" of a given SDA architecture for detecting and tracking cislunar satellites?***

   The measures for detecting the "fitness" of a cislunar SDA architecture are very similar to those of a near-Earth SDA architecture. Performance metrics including detection and tracking are critical, as evidenced by military doctrine. Cost is also of great importance for determining feasibility in system procurement. However, the detection and track metrics for cislunar SDA require modification as they were

not well fitted for a regime with few objects. Because of this, MDOS is replaced with MDT and MMOTG is replaced with MTBT and MTT.

2. ***How can MBSE support evaluation of SDA architectures for detecting and tracking cislunar satellites?***

   The integrated software models developed through this research allowed comparison of several different architectures in an automated fashion. The fitness parameters are a form of decision support tool that can inform future system acquisitions. Additionally, the models allowed physical analysis of the cislunar space domain to provide general understanding of architectural design considerations.

3. ***How do optimized GEO SDA architectures compare to potential cislunar SDA architectures for detecting and tracking cislunar satellites when accounting for system cost?***

   The GEO-optimized SDA architecture developed by Stern and Wachtel performs poorly in comparison to the LEO architectures that were examined. The ground-based telescopes in the former were unable to detect the cislunar object due to the lunar exclusion angle; they did not add to the architecture performance, but they did add to the cost. The synodic LEO architecture provides significantly improved performance at significantly lower cost.

5.4 Future Work

There are three broad areas of future work for this research: Optimization, scenario/architecture expansion, tasking, and cost models.

1. **Optimization Algorithm.** This research manually compared metrics and physical data for each selected architecture to quantitatively determine the best architectures, and to qualitatively understand why they are superior. Following in the footsteps of Stern and Wachtel, this process could be improved by an automated optimization algorithm. This is especially prescient when other parameters are varied, such as aperture size and number of satellites in an orbit.

2. **Additional Object/Observer Locations and Orbits.** This research assessed a single cislunar reference scenario, but there are an infinite number of libration point orbits that could be assessed. If these are not taken into consideration during system design, then the selected cislunar SDA architecture would be optimized only for a point solution, which may or may not be the best general solution. The Lyapunav orbital parameters could be varied, or additional orbits could be assessed, or additional libration points could be used. Additionally, observers could be placed in new locations (e.g., lunar surface, L4/L5, L1/L2).

3. **Tasking Algorithm.** The reference scenario in this research had only one object to be observed. Going forward, as the cislunar domain becomes more congested, it may be appropriate to test the ability of the architecture to detect and track multiple objects simultaneously as was done in Stern and Wachtel. This could be taken a step further, and an integrated near-space

and cislunar SDA architecture could be assessed in its ability to detect and track both GEO and cislunar objects.

4. **Search Function**. This research assumed perfect a priori knowledge of the object state. This may not be appropriate in practice, and it would be useful to understand the implications given the detection gaps in the assessed SDA architectures. This could be done through a probabilistic model that is integrated with the existing software.

5. **Different Model Timeframe.** This research limited the scenario to approximately 14 days, which was the orbital period of the selected Lyapunov orbit. Extending the timeframe of the model to one Synodic period, approximately 39.5 days, may yield different results. Similarly, evaluating the architectures at different times of year to account for seasonal inclination differences between the synodic, Earth equatorial, and ecliptic planes could prove useful.

6. **Addition of Albedo Effects**. The architectures that performed will in this research did so because the Earth blocked moonlight, preventing sensor saturation. However, this research did not take into account Earth exclusion angles due to the Earth albedo. This should be examined, as it could drastically change the results. Similarly, the Earth and Lunar albedo effects should be included in observer SNR calculations.

7. **Updated Cost Models.** Emerging space operating concepts and technologies could change the cost models. Proliferated LEO constellations, cheap access to space, and hosted payloads are all disruptive to traditional cost estimation, and could prove useful in determining the best path forward in procuring a cislunar SDA system.

5.5 Summary

Overall, the MBSE software developed for this research achieved its purpose. The results here-in can be used immediately to better educate an agency such as the Space Development Agency that aims to procure a cislunar SDA system. The discovery that the Earth can assist with cislunar SDA by blocking the Moon from the sensor field of view could be of particular use. However, while this research presents useful results, it more importantly lays a foundation for a significant amount of future work in this burgeoning field.

Appendix A: Physical Constants

The following physical constants were reproduced from Parker and Anderson (2013):

D_m	Mean distance between Earth and Moon	384400	km
G	Universal gravitational constant	6.673×10^{-20}	$km^3/s^2/kg$
GM_e	Gravitational parameter of Earth	398600.432897	km^3/s^2
GM_m	Gravitational parameter of Moon	4902.800582	km^3/s^2

Appendix B: Object Parameters

Reflectivity (aluminum)	C_D	0.88
Shape		Sphere
Size (radius)	r_{serv}	1 m

Appendix C: SDA Sensor Information

Ground Telescope Sensor Properties

Quantum Efficiency	η	0.65
Optical Throughput	τ_{OPT}	0.9
Integration Time	t_{INT}	1 sec
Average Wavelength	λ_{avg}	600 nm
Aperture Diameter	A_{RCVR}	1 m
Read Noise	N_r	12 e/pixel
Dark Noise	N_d	6 e/pixel/sec
Minimum Elevation Angle	20	Degrees
Solar Exclusion Angle	40	Degrees
Lunar Exclusion Angle	10	Degrees

Ground Telescope Locations

Location	**Lat (deg)**	**Long (deg)**	**Alt (m)**	$\boldsymbol{\tau_{ATM}}$
Diego Garcia	7.32	72.42	0	0.79
Haleakala, HI	20.71	-156.26	3052	0.91
La Palma, Canary Islands	28.73	-17.90	2396	0.90
Mauna Kea, HI	19.82	-155.47	4205	0.93
IAO	32.78	78.96	4500	0.95
Mount Graham, AZ	32.70	-109.89	3191	0.91
Paranal, Chile	-24.59	-70.19	2635	0.91
Siding Spring, Australia	-31.26	149.05	1165	0.86
Socorro, NM	33.82	-106.66	3230	0.92

LEO and GEO Satellite Sensor Properties

Quantum Efficiency	η	0.65
Optical Throughput	τ_{OPT}	0.9
Integration Time	t_{INT}	1 sec
Average Wavelength	λ_{avg}	600 nm
Aperture Diameter	A_{RCVR}	0.3 m
Read Noise	N_r	12 e/pixel
Dark Noise	N_d	6 e/pixel/sec
Solar Exclusion Angle	40	Degrees
Lunar Exclusion Angle	5	Degrees

Appendix D: Test Case Graphs

		GEO	LEO	Ground
Reference Comparisons				
1	Stern & Wachtel (Optimized)	Yes		
GEO and LEO comparison				
2	GEO and LEO	Yes	Yes	NA
3	GEO (polar/equatorial)	Yes	NA	NA
4	GEO (polar)	Yes	NA	NA
5	GEO (equatorial)	Yes	NA	NA
6	GEO (synodic)	Yes	NA	NA
7	LEO (polar/equatorial)	NA	Yes	NA
8	LEO (polar)	NA	Yes	NA
9	LEO (equatorial)	NA	Yes	NA
10	LEO (synodic)	NA	Yes	NA

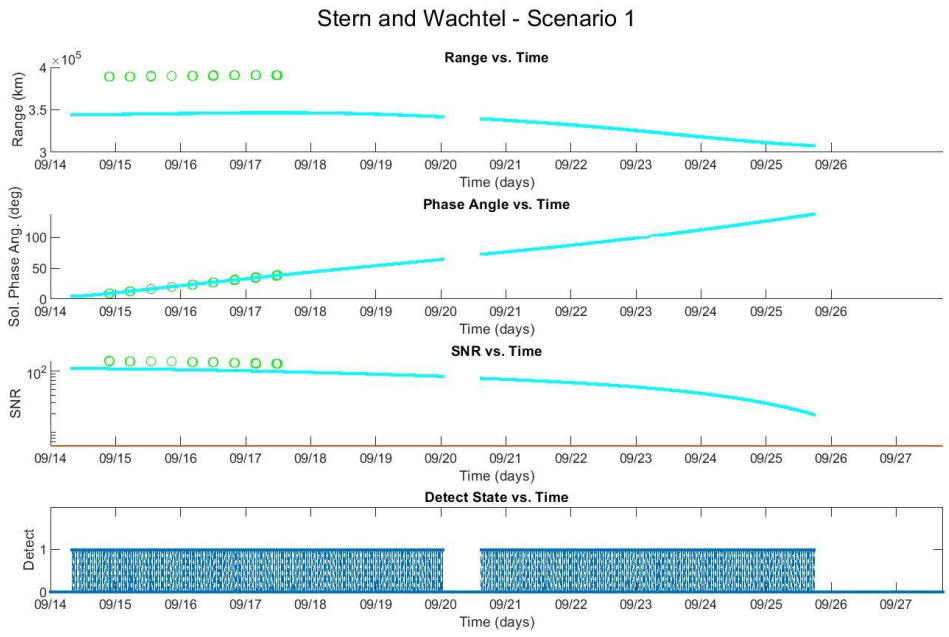

Results for Stern and Wachtel in Scenario 1

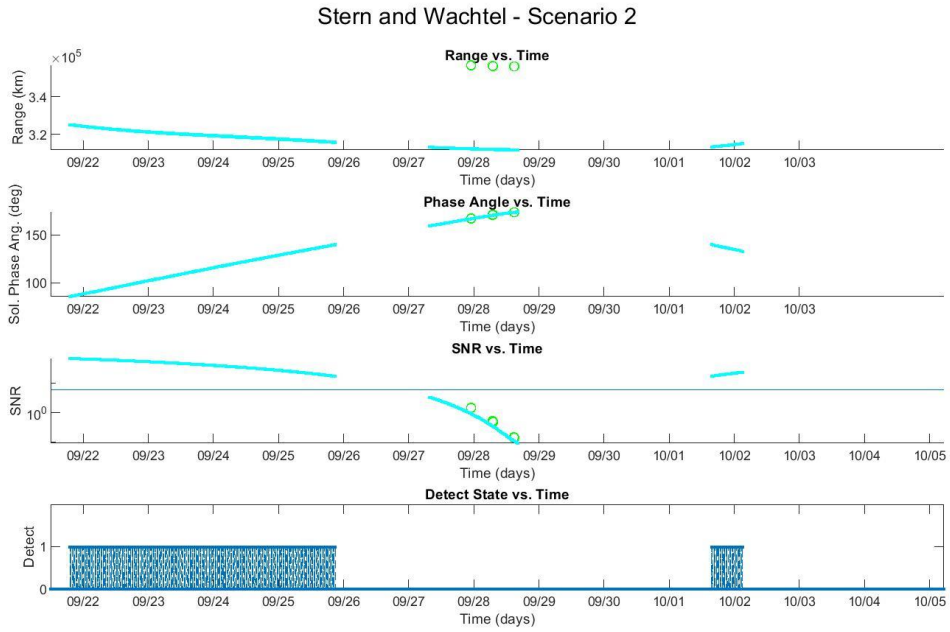

Results for Stern and Wachtel in Scenario 2

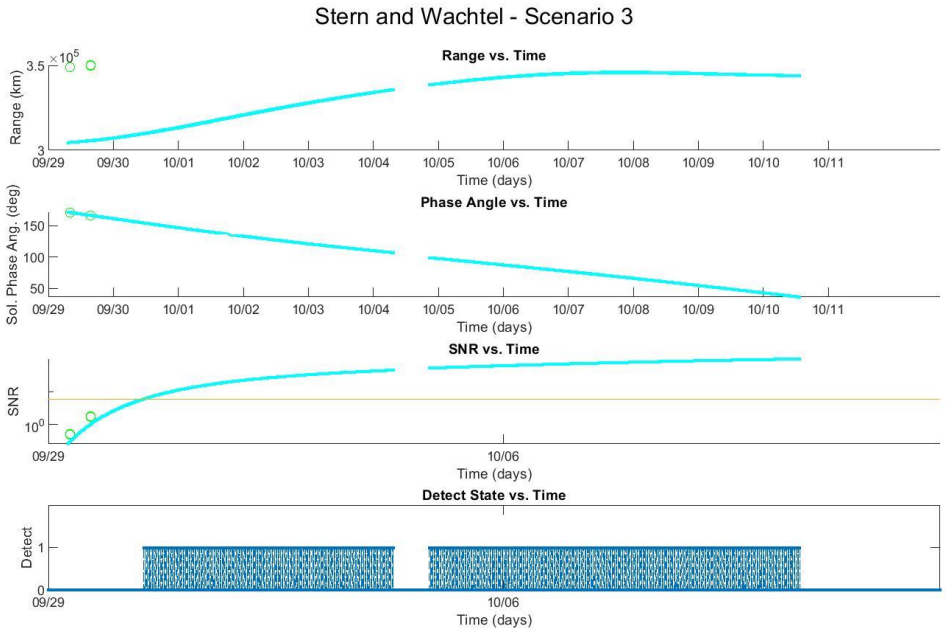

Results for Stern and Wachtel in Scenario 3

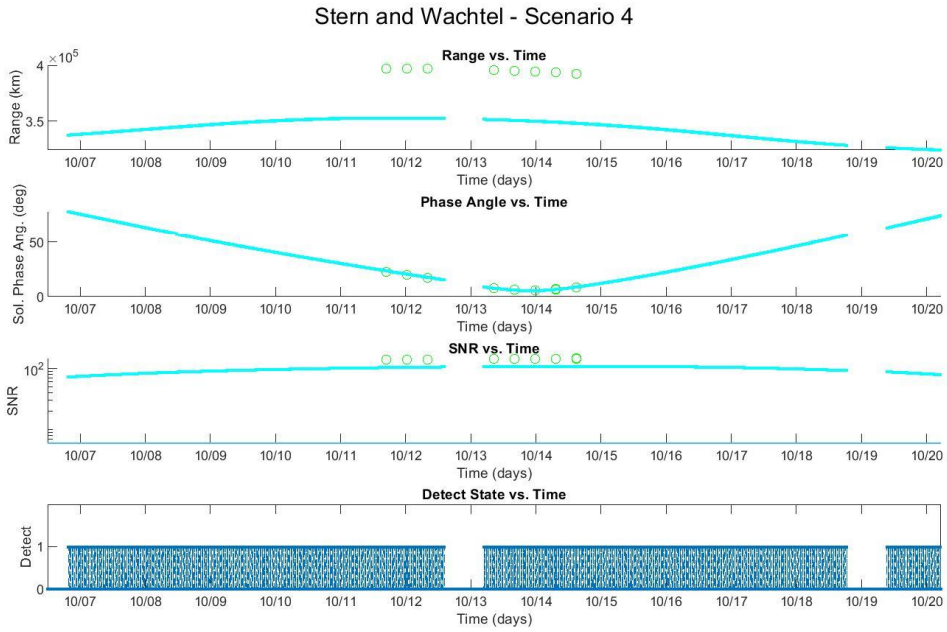

Results for Stern and Wachtel in Scenario 4

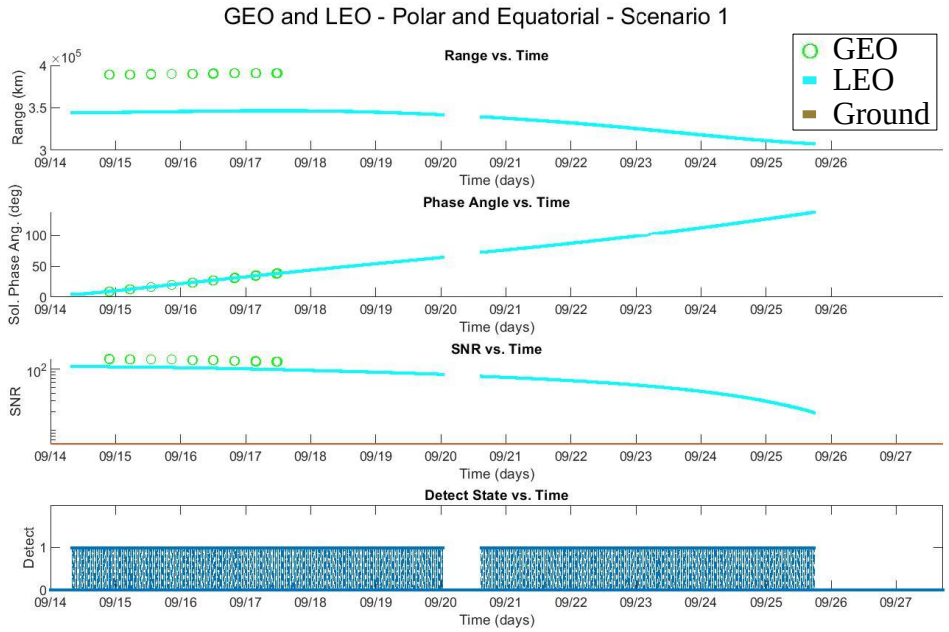

Results for GEO (polar and eq) and LEO (polar and eq) Constellations in Scenario 1

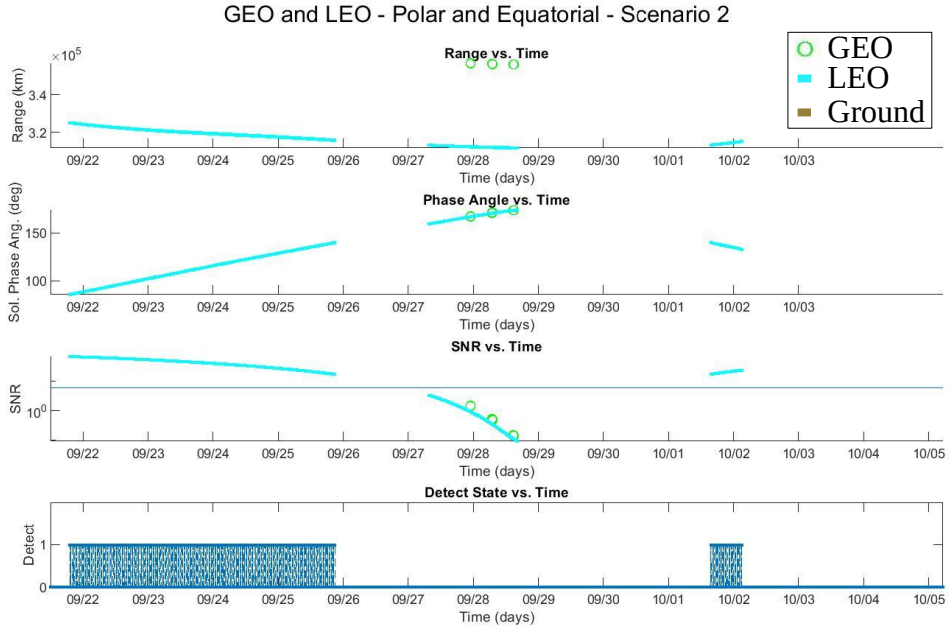

Results for GEO (polar and eq) and LEO (polar and eq) Constellations in Scenario 2

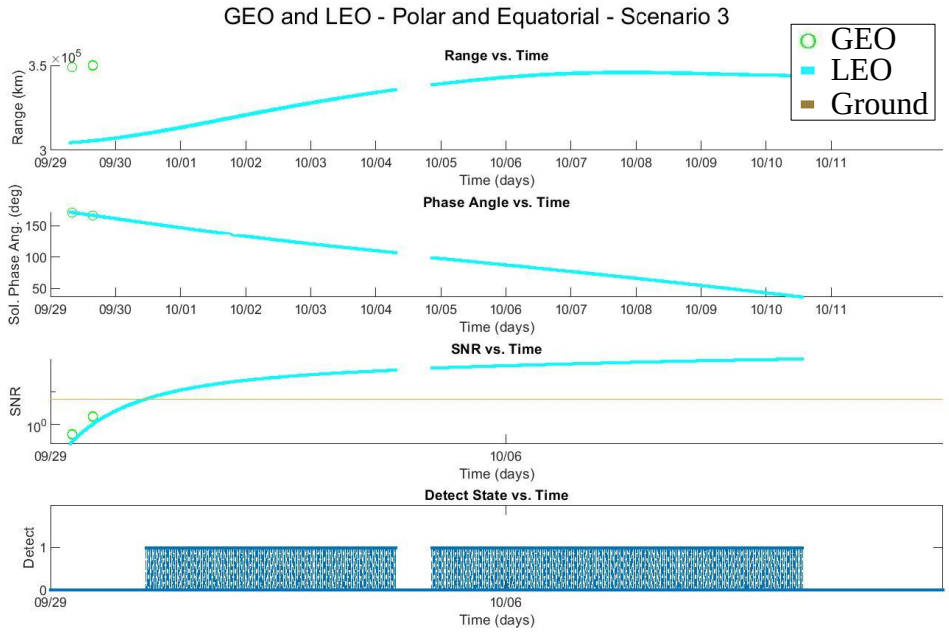

Results for GEO (polar and eq) and LEO (polar and eq) Constellations in Scenario 3

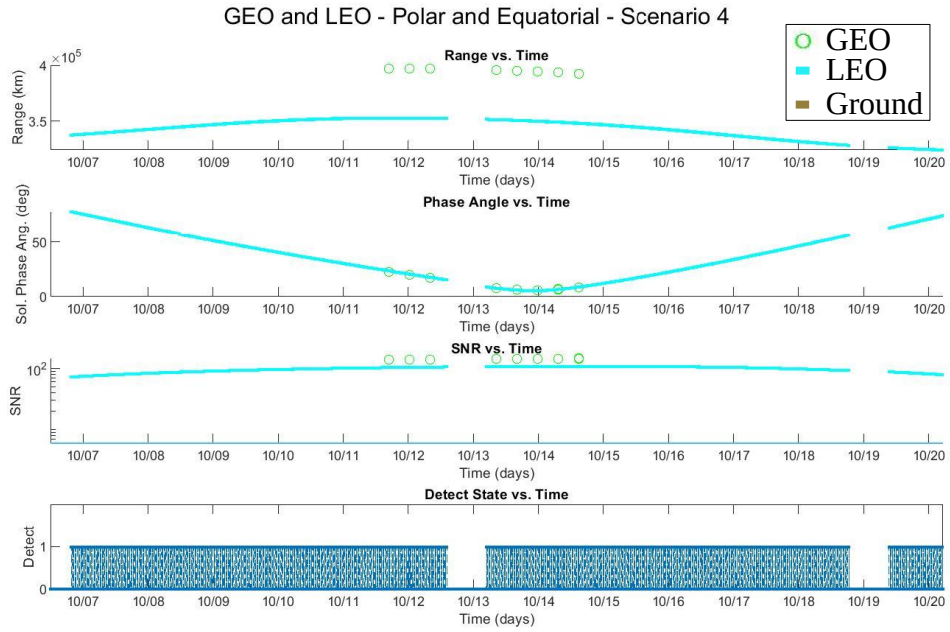

Results for GEO (polar and eq) and LEO (polar and eq) Constellations in Scenario 4

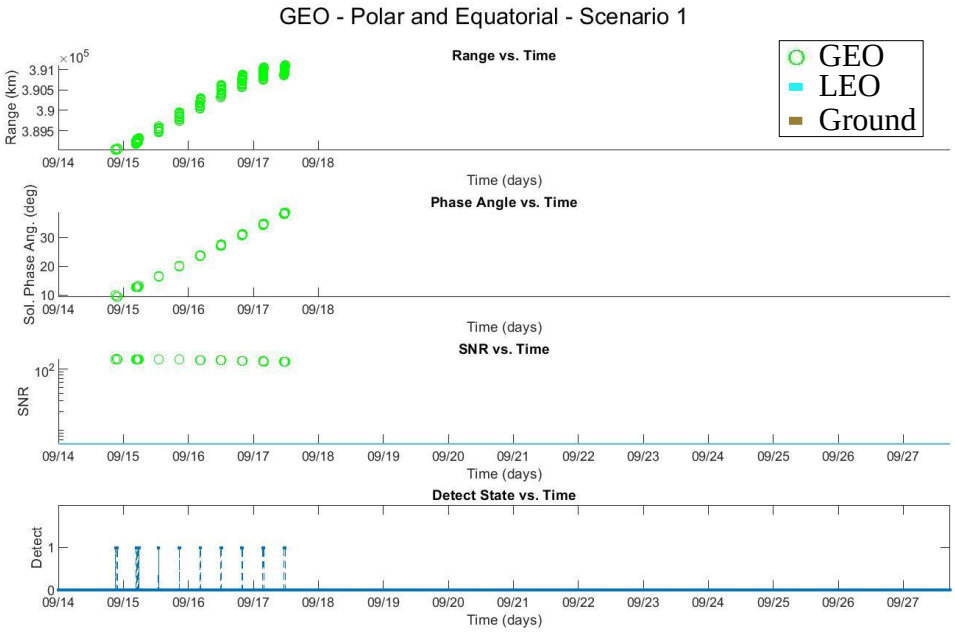

Results for GEO (polar and equatorial) Constellations in Scenario 1

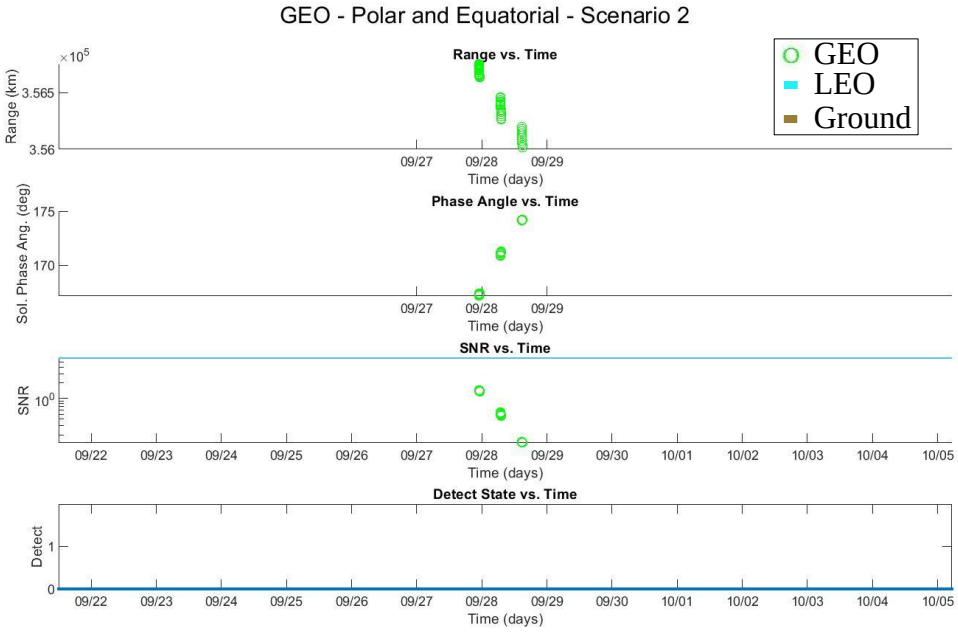

Results for GEO (polar and equatorial) Constellations in Scenario 2

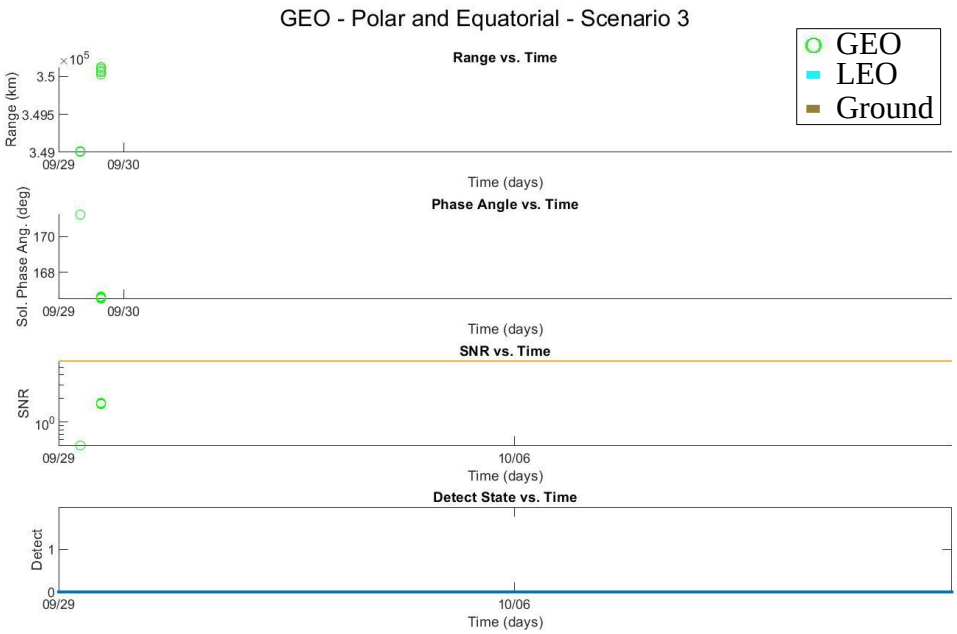

Results for GEO (polar and equatorial) Constellations in Scenario 3

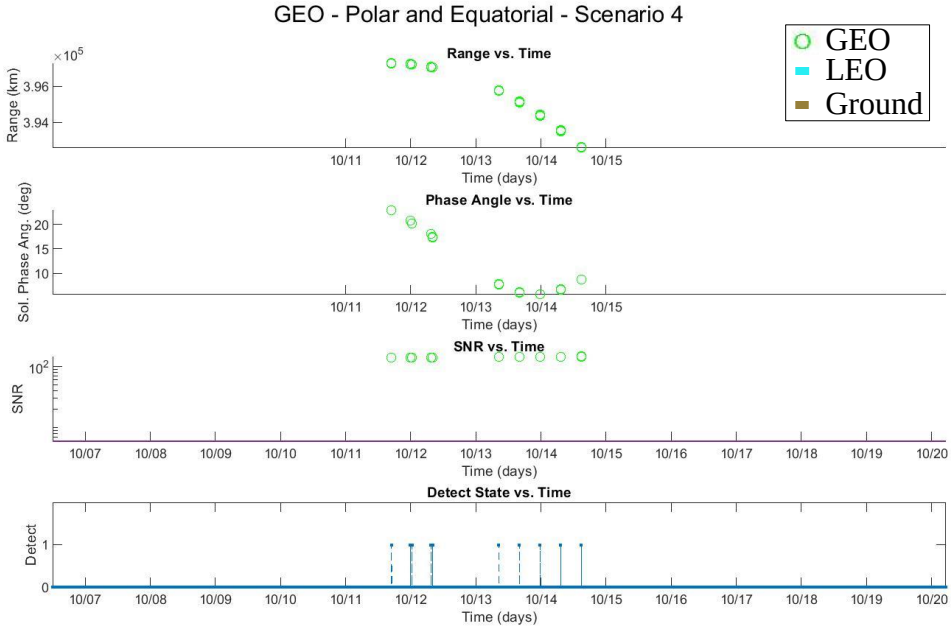

Results for GEO (polar and equatorial) Constellations in Scenario 4

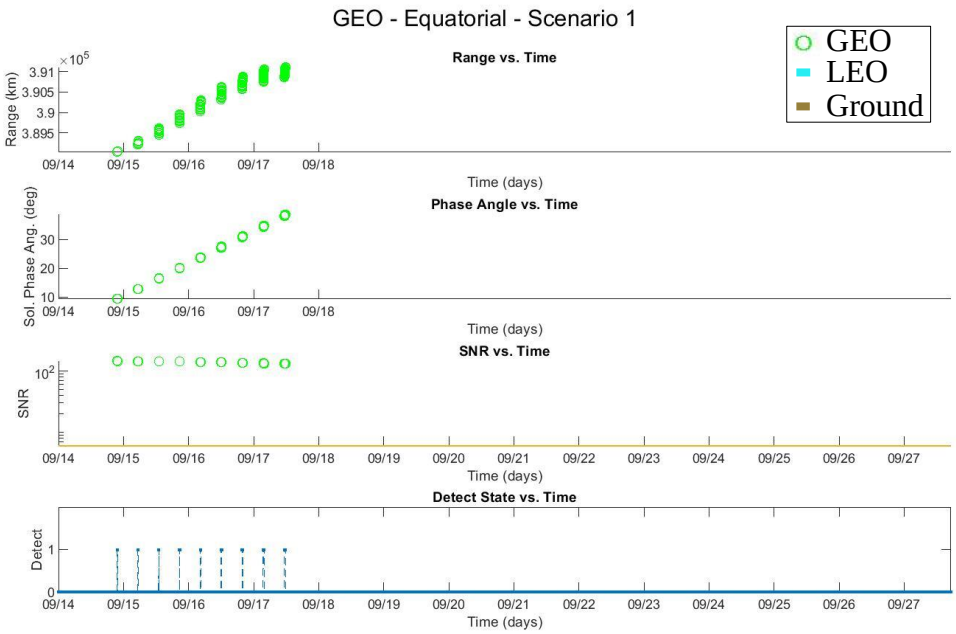

Results for GEO (equatorial) Constellations in Scenario 1

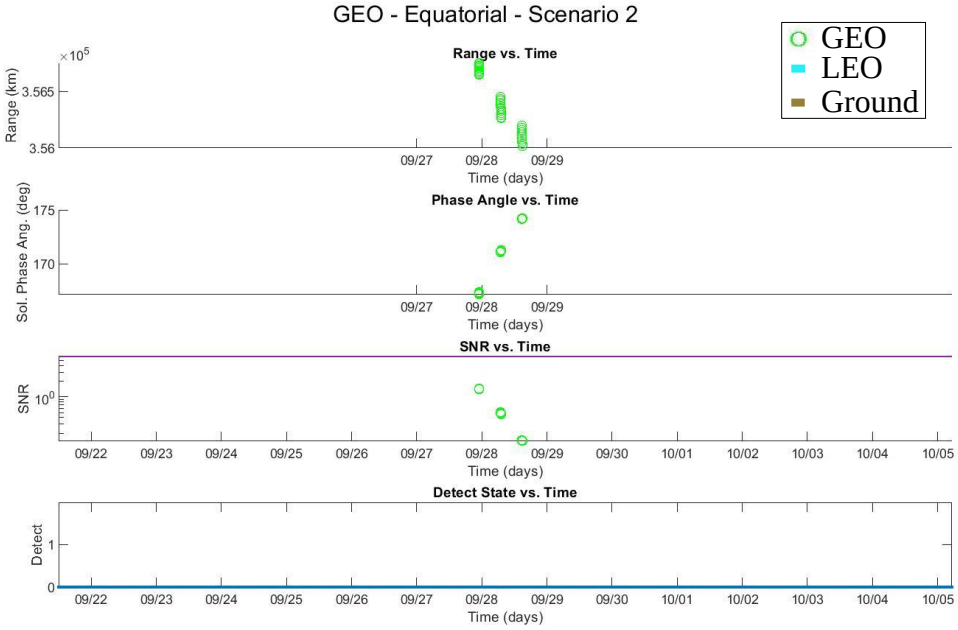

Results for GEO (equatorial) Constellations in Scenario 2

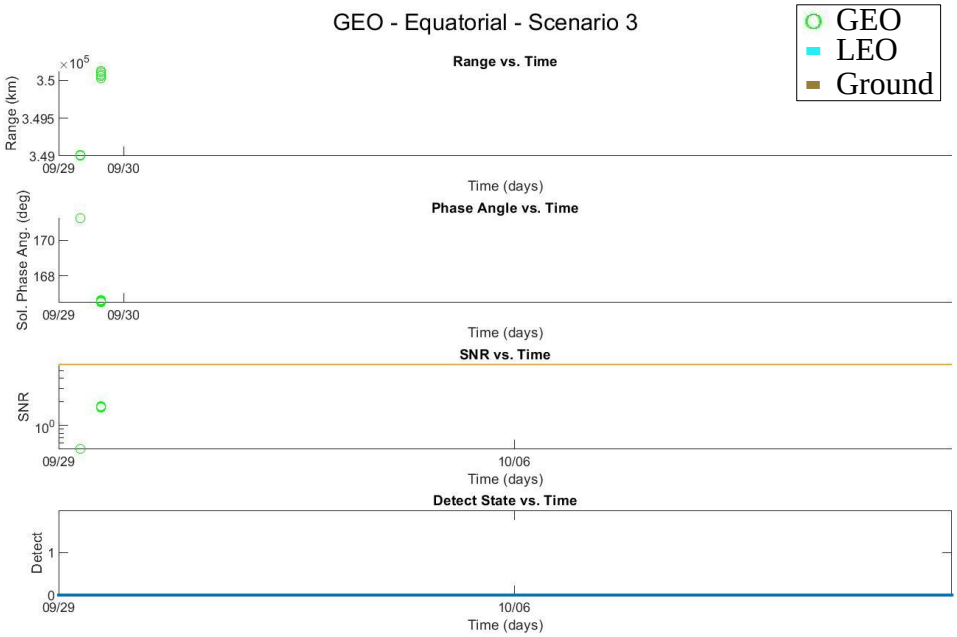

Results for GEO (equatorial) Constellations in Scenario 3

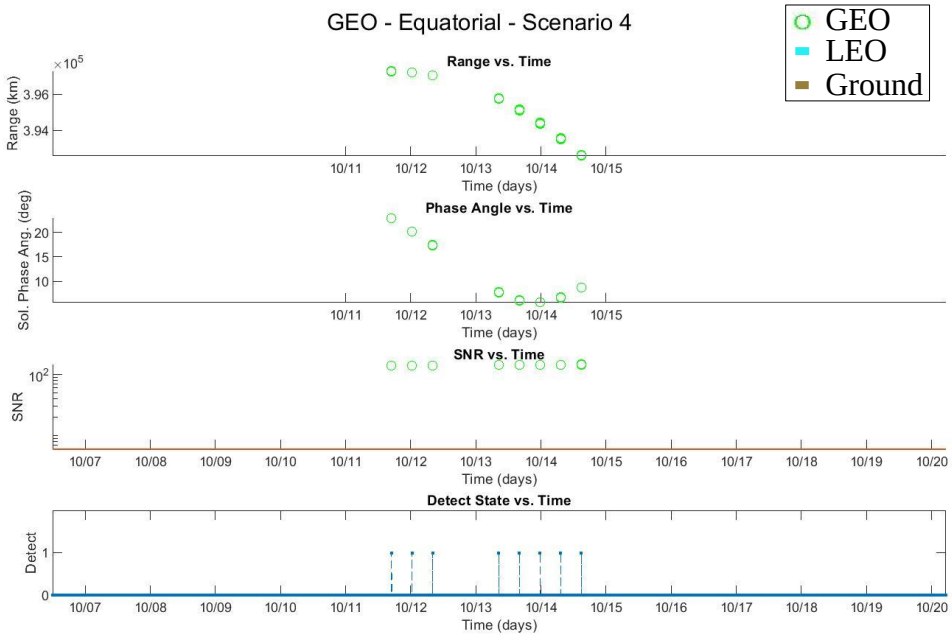

Results for GEO (equatorial) Constellations in Scenario 4

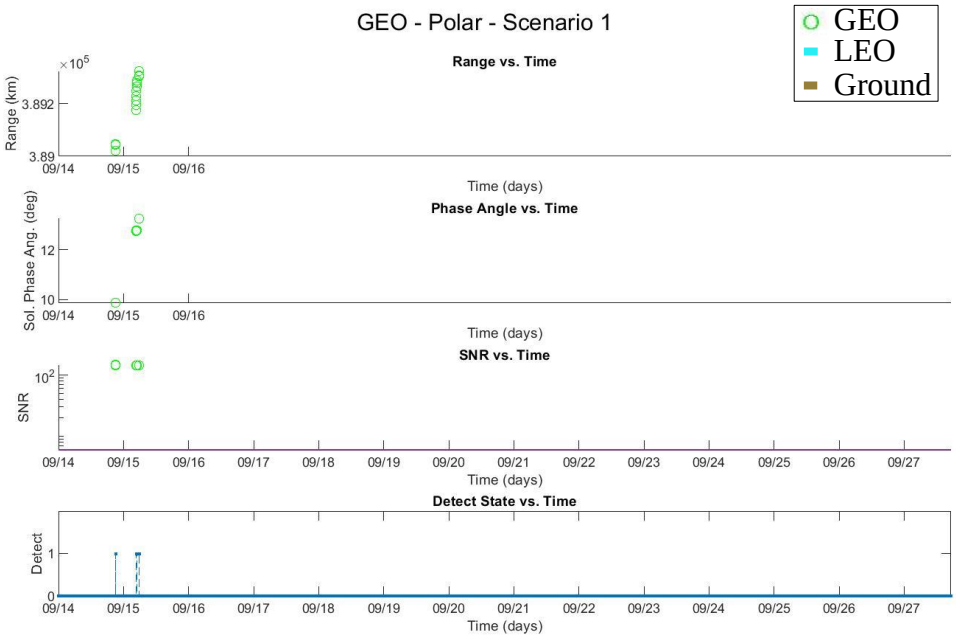

Results for GEO (polar) Constellations in Scenario 1

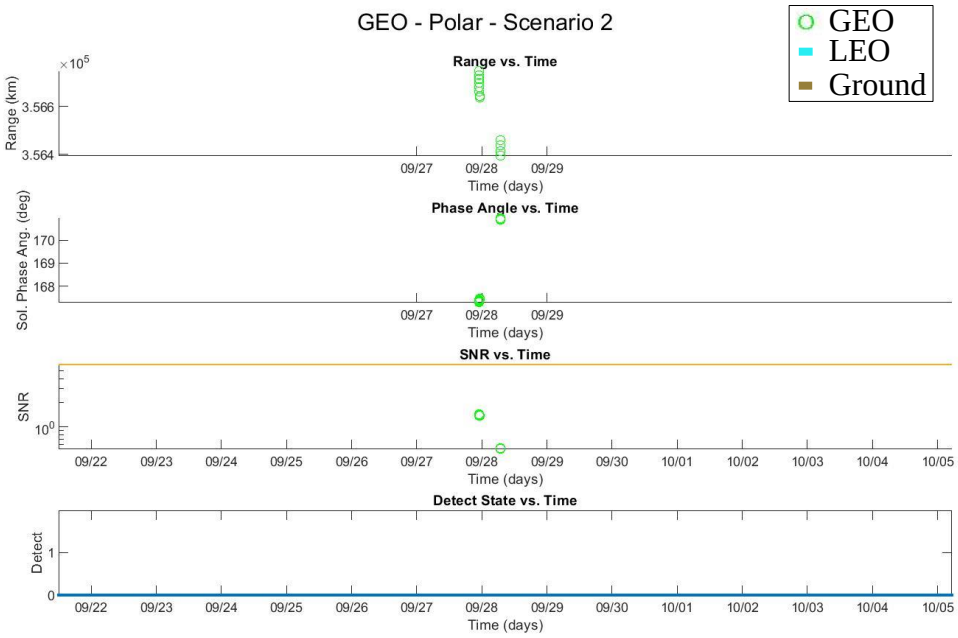

Results for GEO (polar) Constellations in Scenario 2

Results for GEO (polar) Constellations in Scenario 3

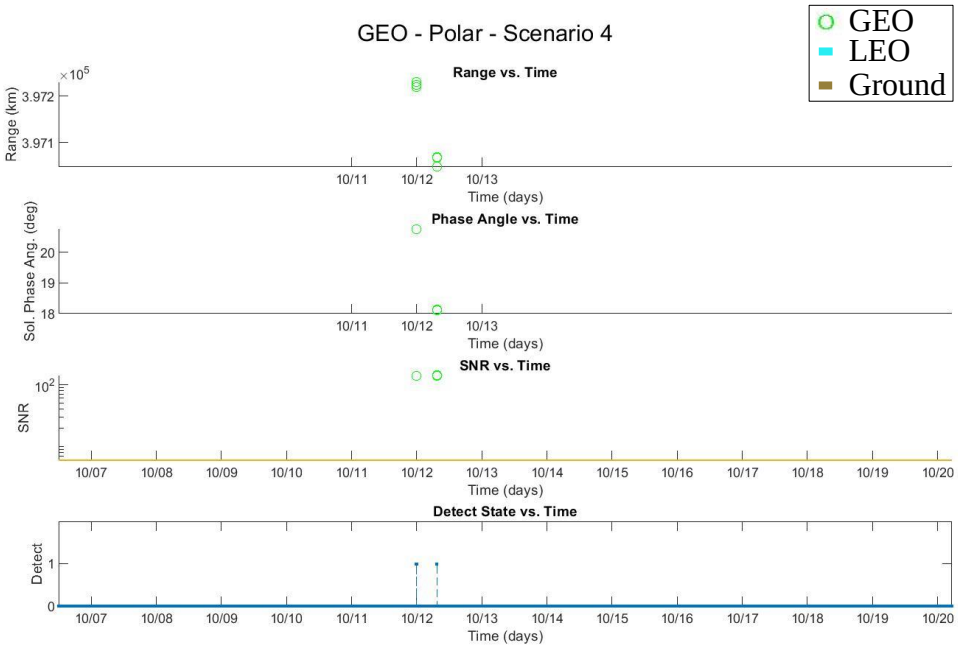

Results for GEO (polar) Constellations in Scenario 4

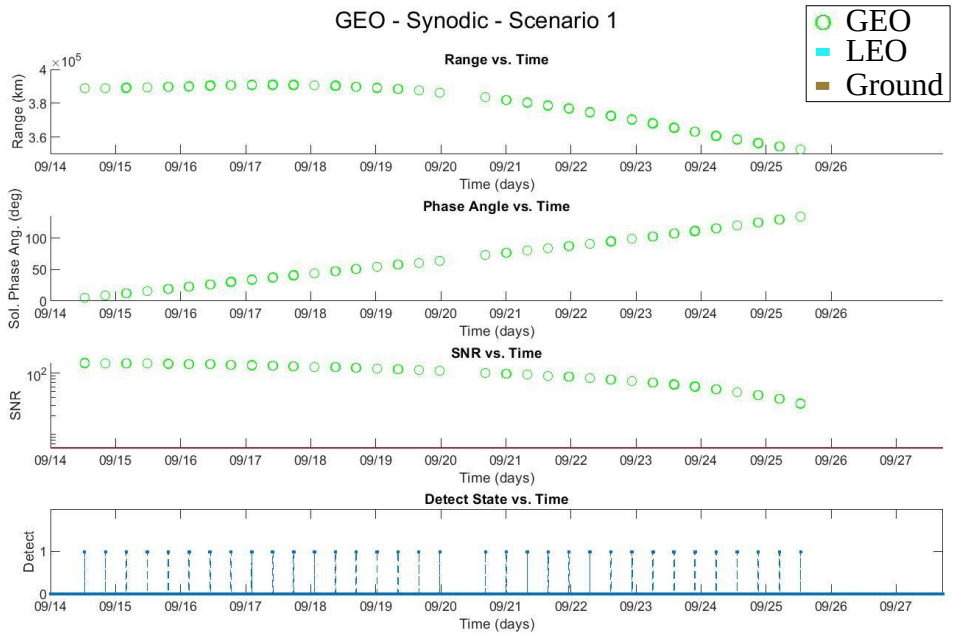

Results for GEO (synodic) Constellations in Scenario 1

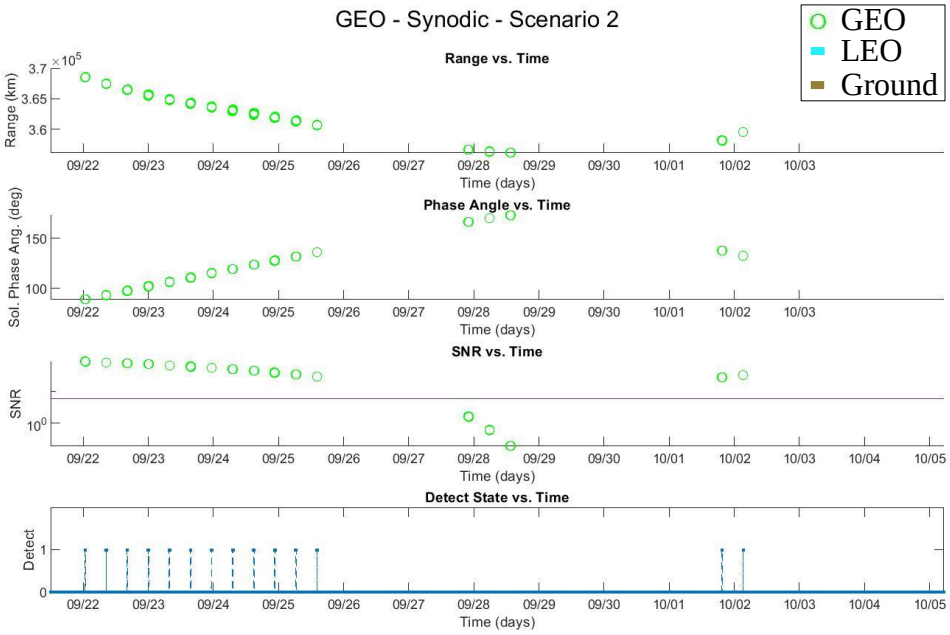

Results for GEO (synodic) Constellations in Scenario 2

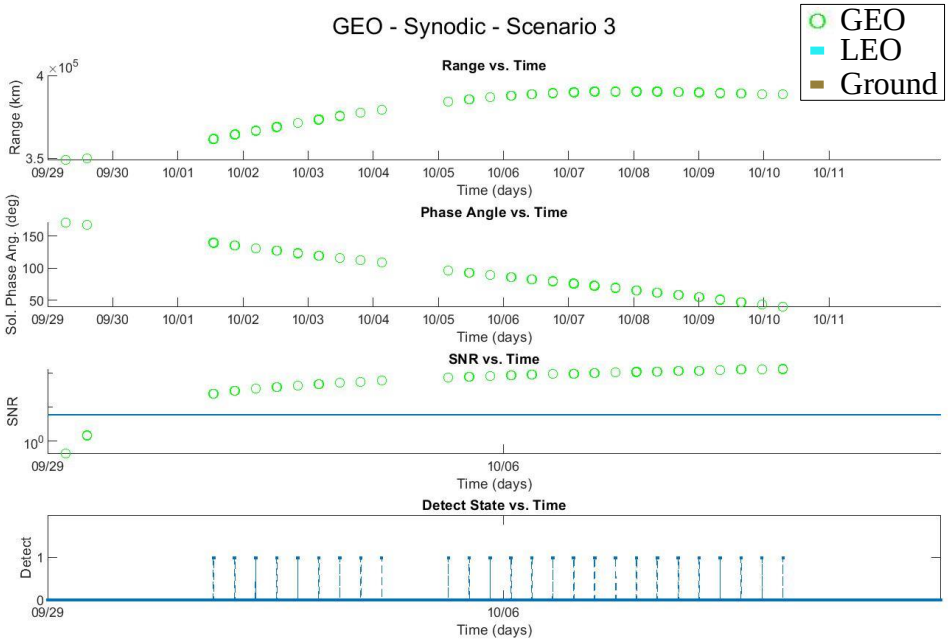

Results for GEO (synodic) Constellations in Scenario 3

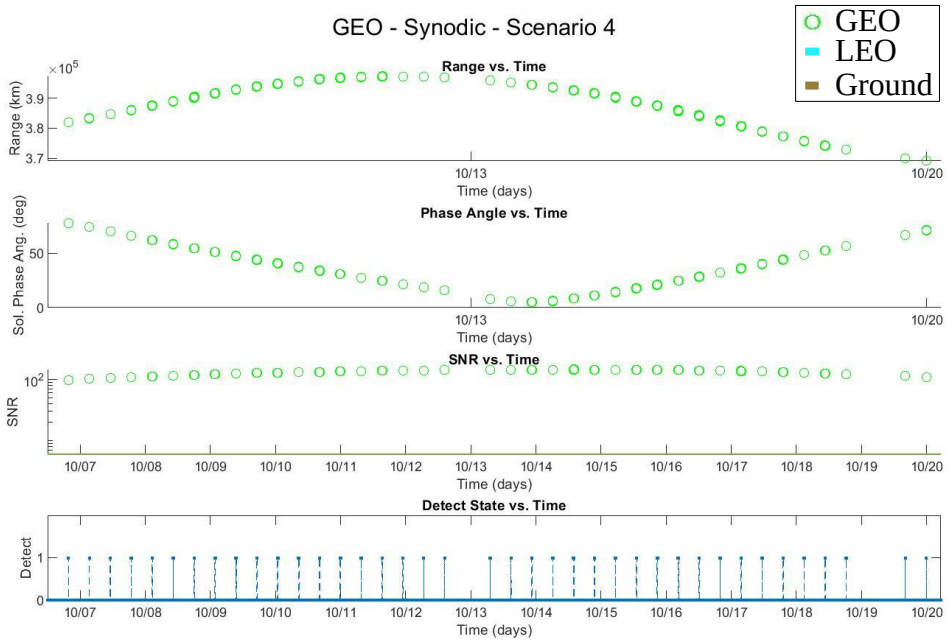

Results for GEO (synodic) Constellations in Scenario 4

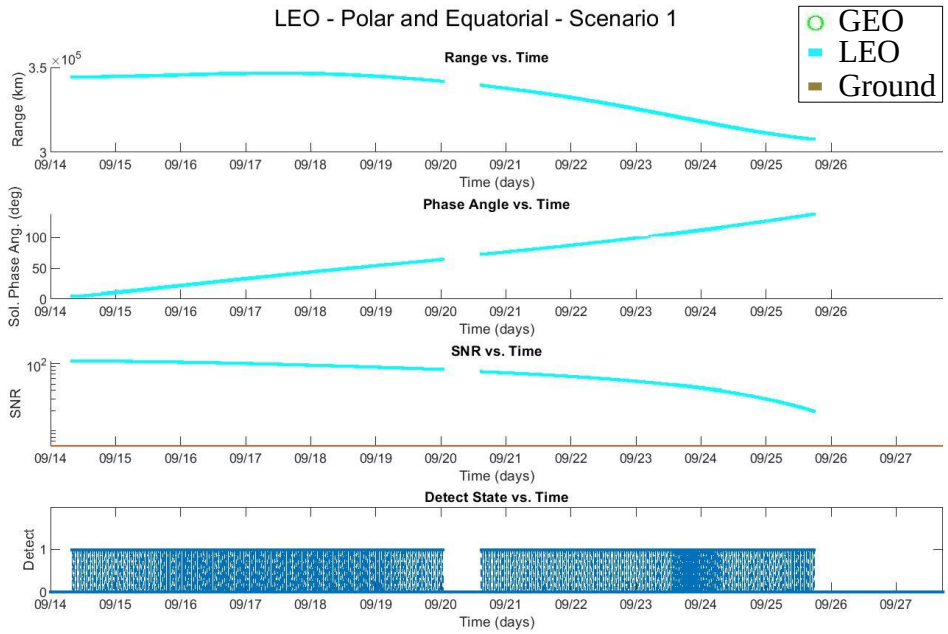

Results for LEO (polar and equatorial) Constellations in Scenario 1

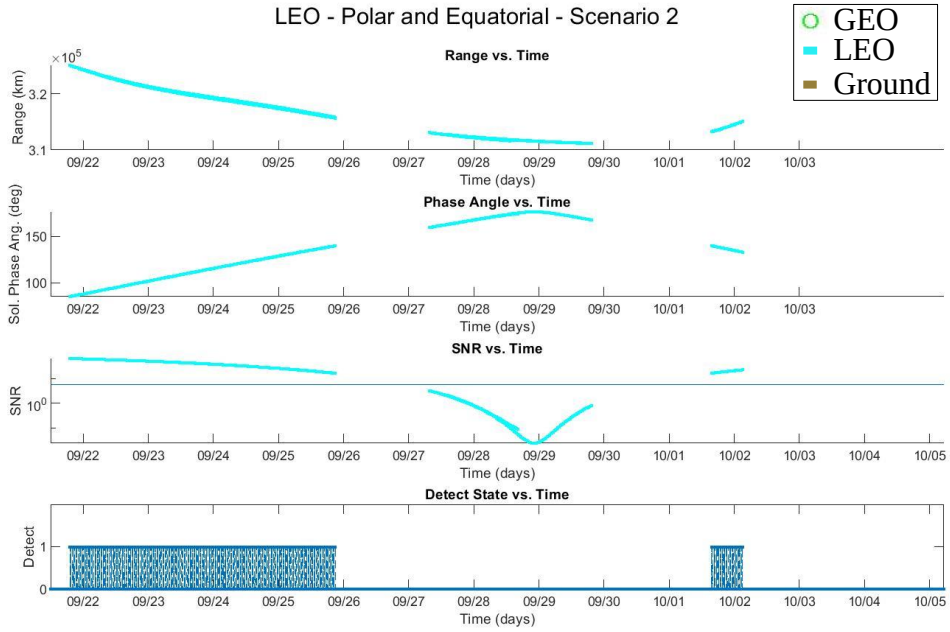

Results for LEO (polar and equatorial) Constellations in Scenario 2

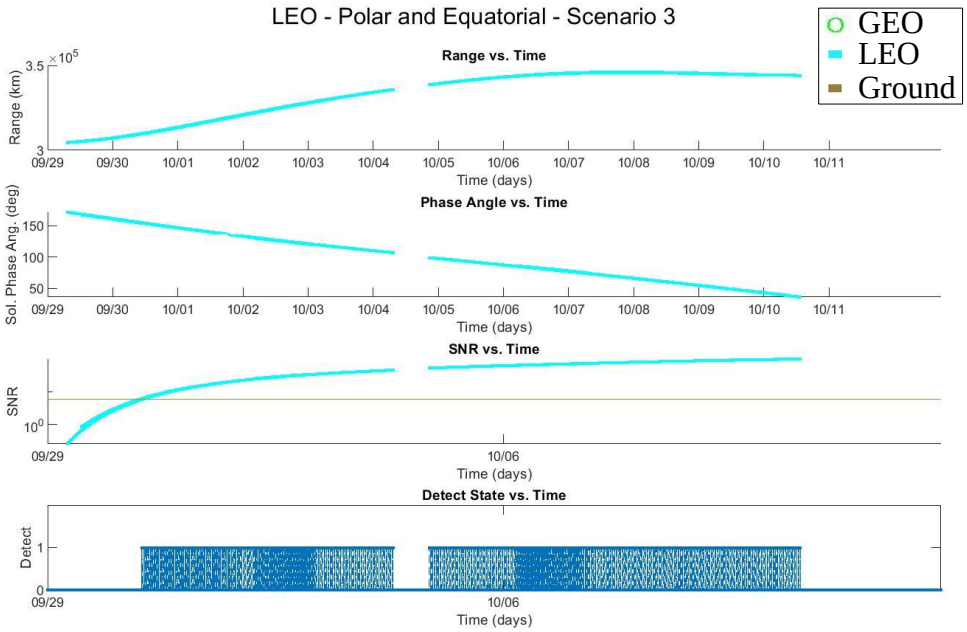

Results for LEO (polar and equatorial) Constellations in Scenario 3

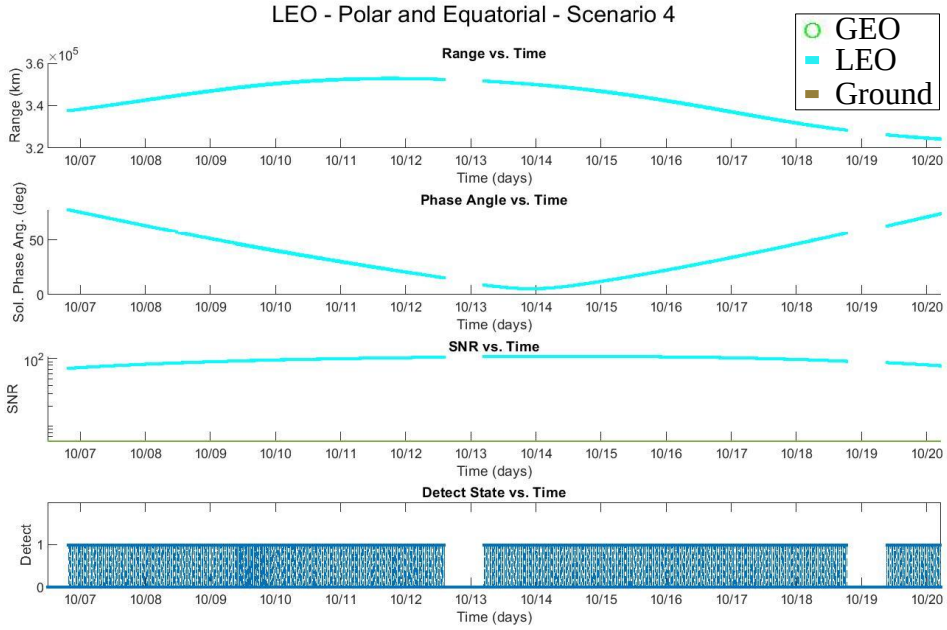

Results for LEO (polar and equatorial) Constellations in Scenario 4

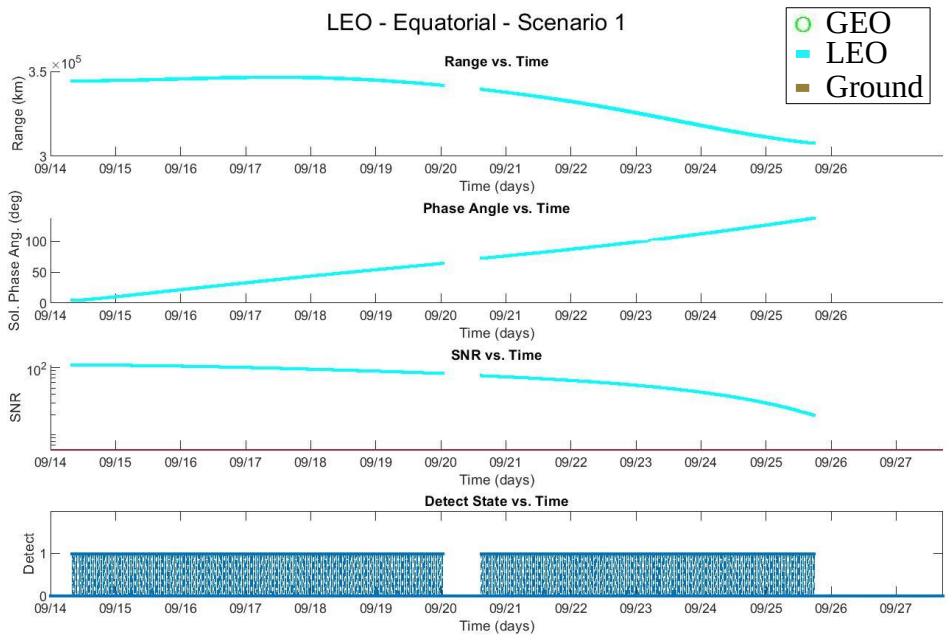

Results for LEO (equatorial) Constellations in Scenario 1

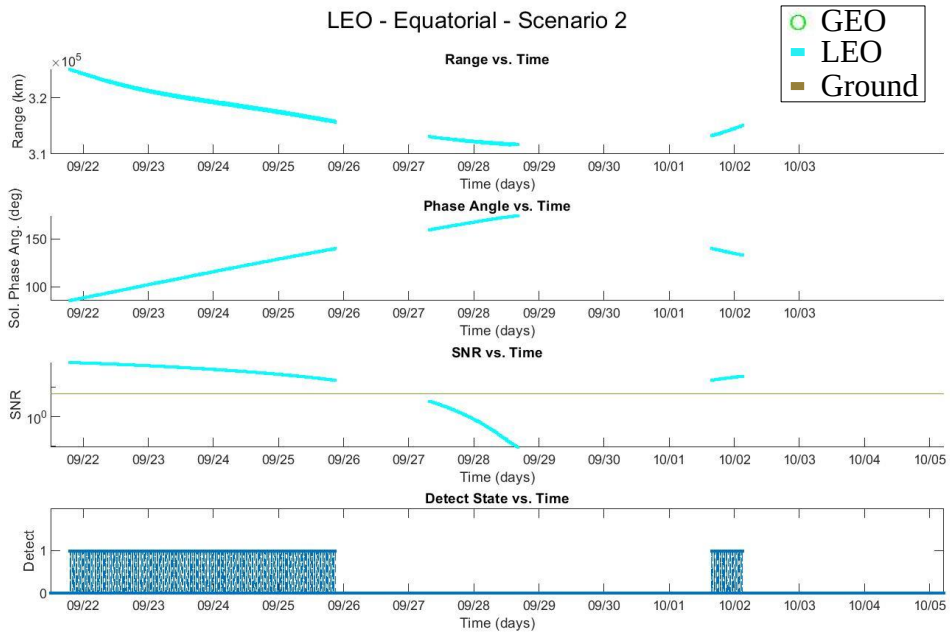

Results for LEO (equatorial) Constellations in Scenario 2

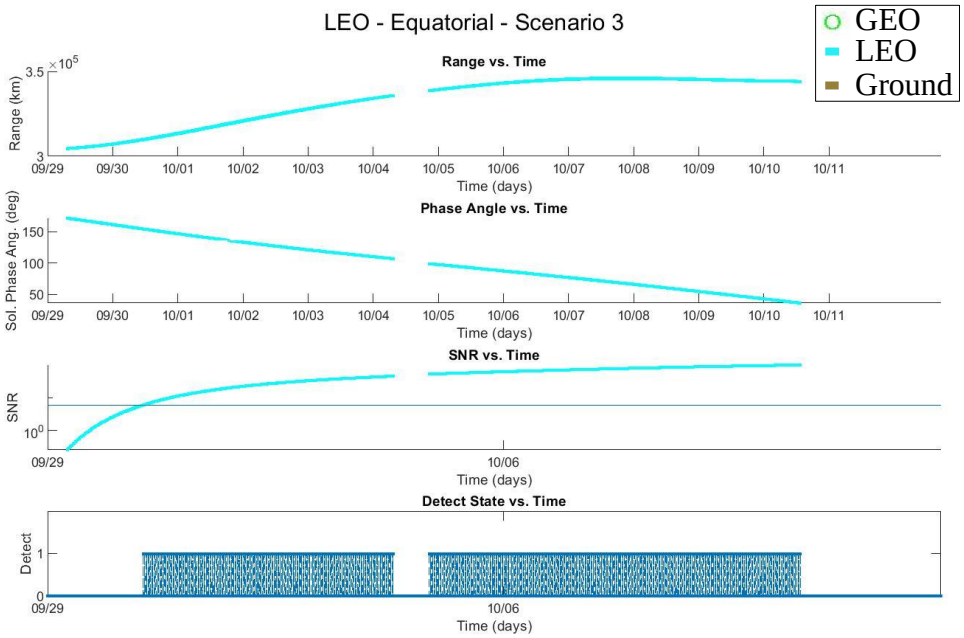

Results for LEO (equatorial) Constellations in Scenario 3

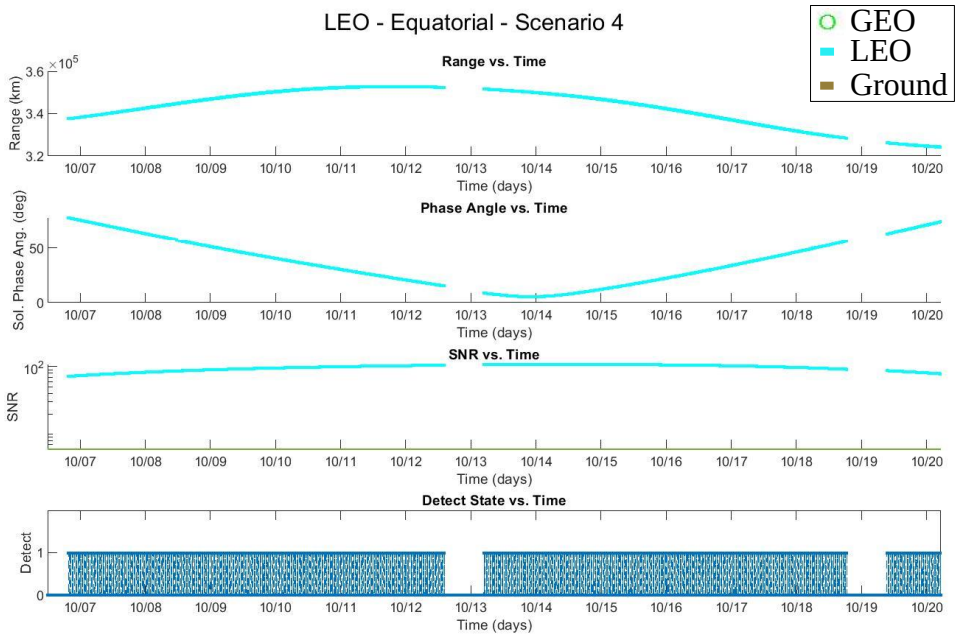

Results for LEO (equatorial) Constellations in Scenario 4

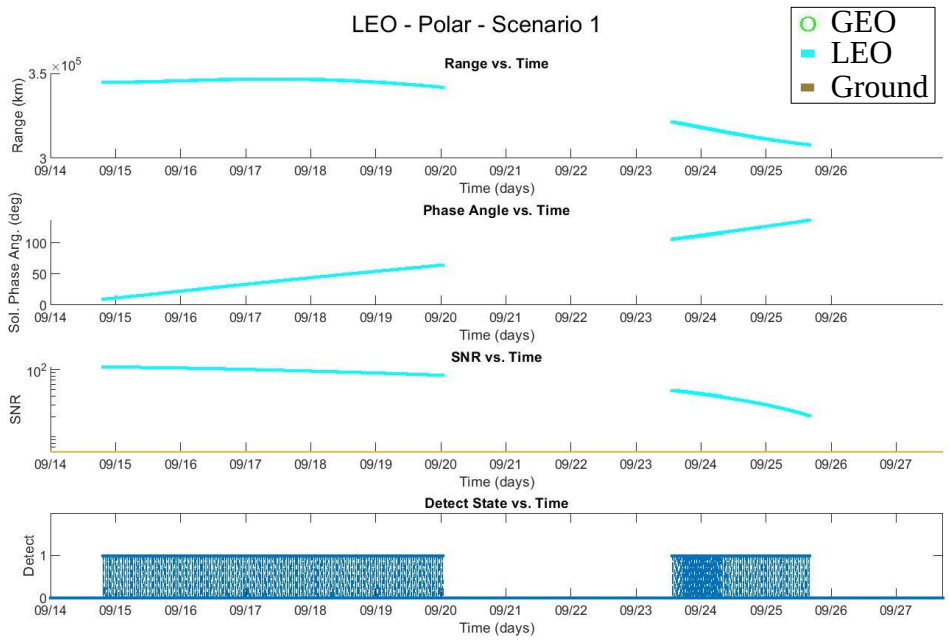

Results for LEO (polar) Constellations in Scenario 1

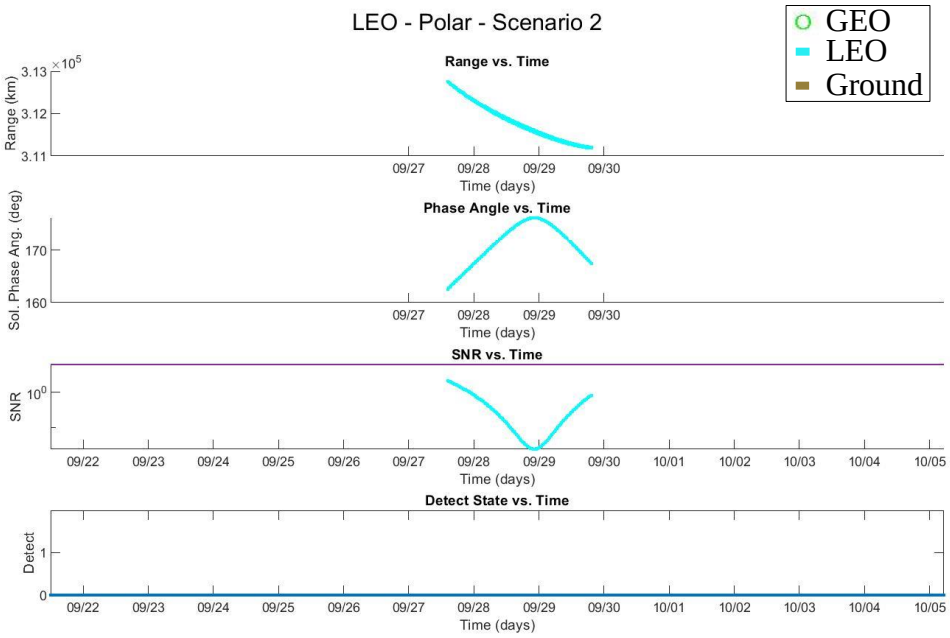

Results for LEO (polar) Constellations in Scenario 2

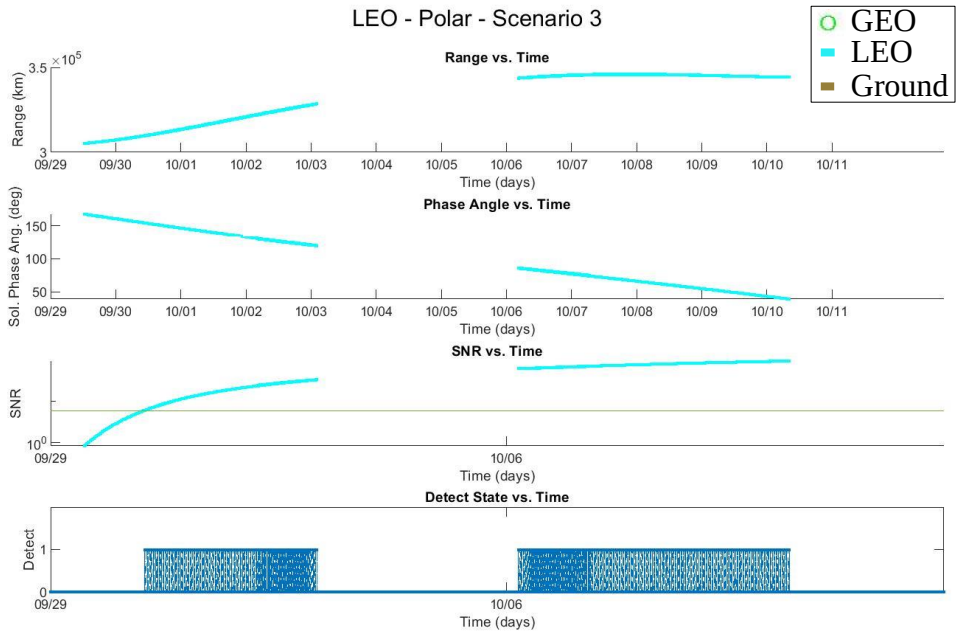

Results for LEO (polar) Constellations in Scenario 3

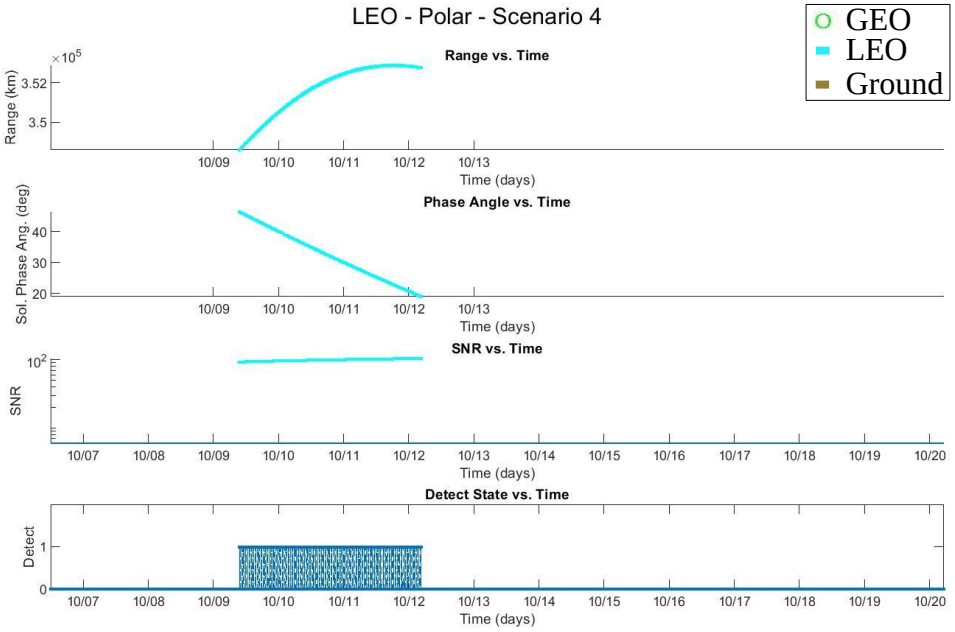

Results for LEO (polar) Constellations in Scenario 4

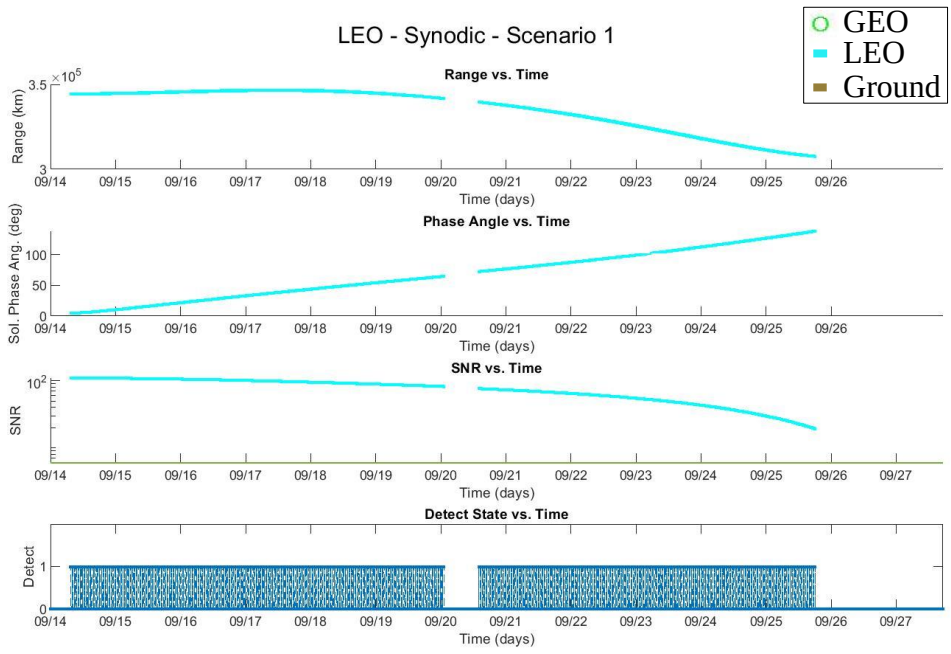

Results for LEO (synodic) Constellations in Scenario 1

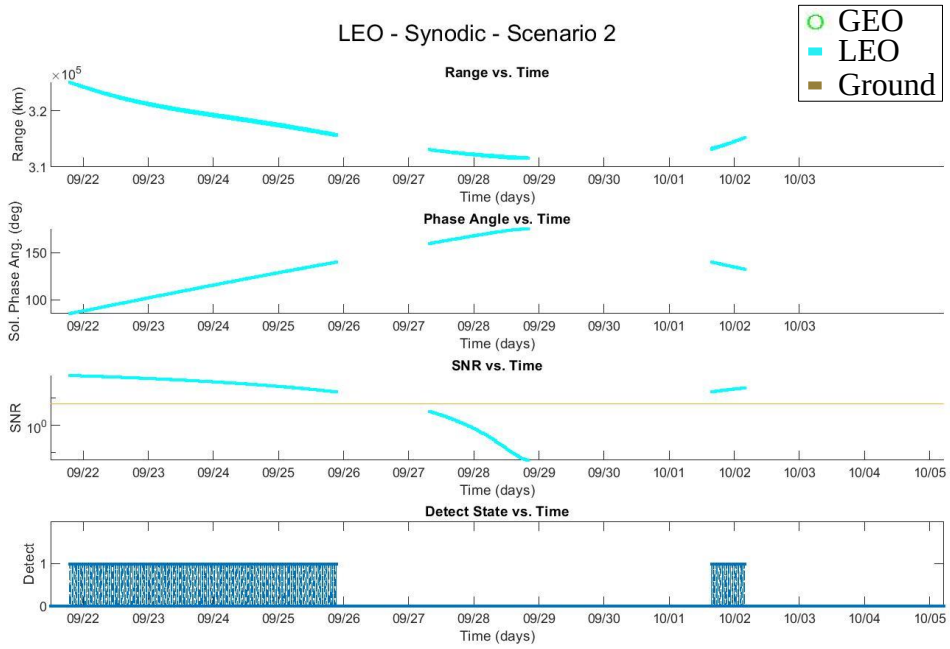

Results for LEO (synodic) Constellations in Scenario 2

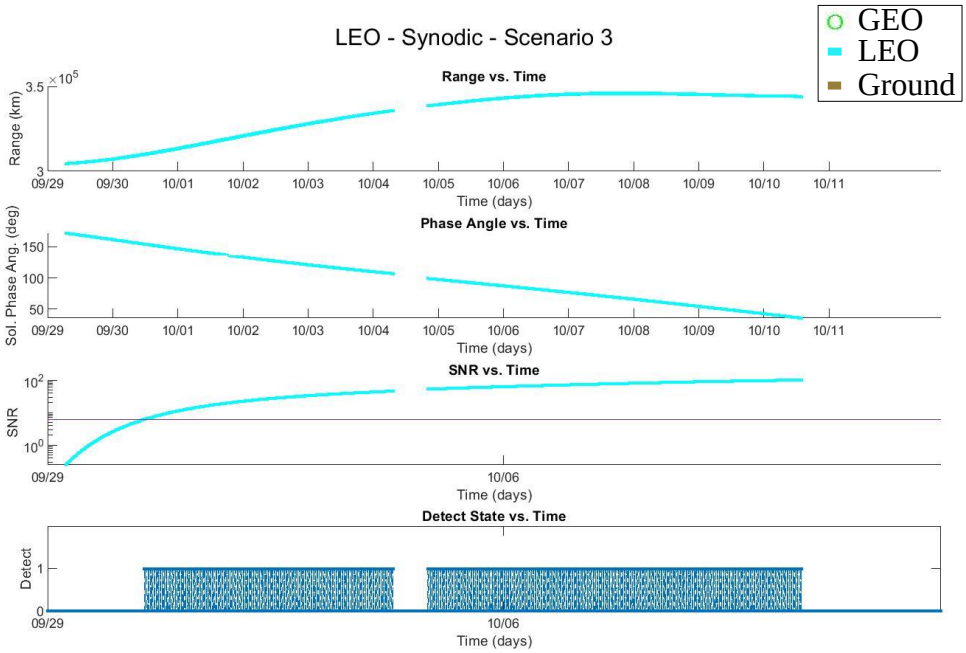

Results for LEO (synodic) Constellations in Scenario 3

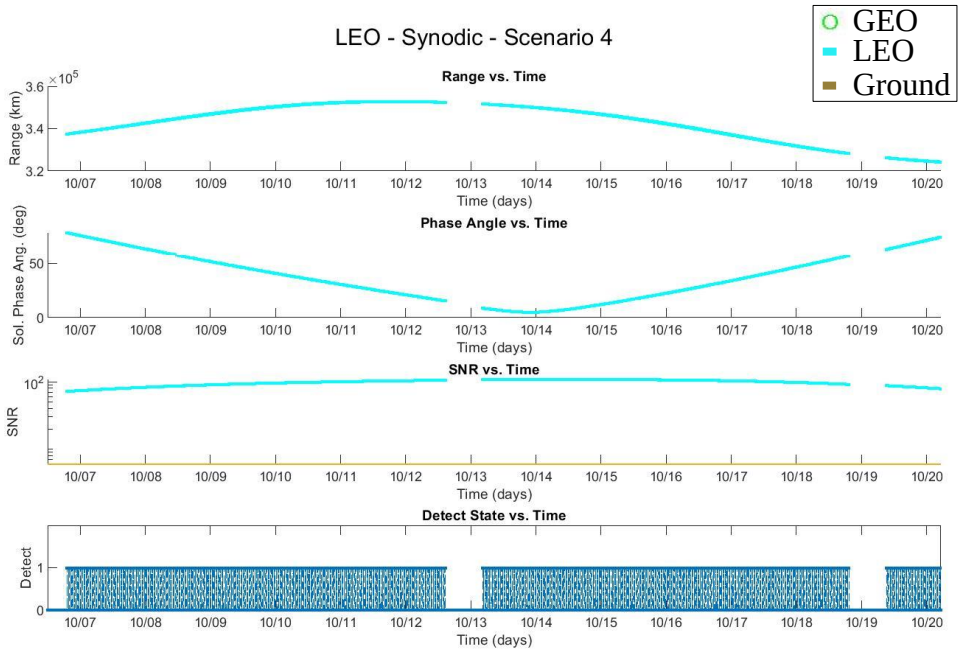

Results for LEO (synodic) Constellations in Scenario 4

Bibliography

Ackermann, M. R., Kiziah, R. R., Zimmer, P. C., McGraw, J. T., Cox, D. D. (2015). *A Systematic Examination of Ground-Based and Space –Based Approaches to Optical Detection and Tracking of Satellites.*

Adams, D. (1980). *The Hitchhiker's Guide to the Galaxy.* Pan Books

AGI (2019). Vehicle Local Coordinate Axes. Retrieved from http://help.agi.com/stk/index.htm#gator/eq-coordsys.htm . Accessed 16 May 2019.

Bartels, M. (2019). Russia and China are teaming up to explore the moon. Retrieved from https://www.space.com/russia-china-moon-exploration-partnership.html

Bate, R. R., Mueller, D. D., White, J. E. (1971) *Fundaentals of Astrodynamics*. New York, New York: Dover Publications.

Coakley, J. A. (2003) *Reflectance and Albedo, Surface*. Encyclopedia of Atmospheric Sciences.

Collette, Y. and Siarry, P. (2003). *Multiobjective Optimization: Principles and Case Studies.* Berlin: Springer

Farquhar, R. W. and Kamel, A. A. (1972). Quasi-periodic Orbits around the Translunar Libration Point. *Celestial Mechanics* 458(7)

Felten, M. S. (2018) *Optimization of Geosynchronous Space Situational awareness Architectures Using Parallel Computing.* Air Force Institute of Technology.

Grebow, D. J. (2006). *Generating Periodic Orbits in the Circular Restricted Threebody Problem with Applications to Lunar South Pole Coverage*. Purdue University.

Hitchens, T. (2019). *SDA's Kennedy: Cislunar Space the Next Military Frontier*. Retrieved from https://breakingdefense.com/2019/04/sdas-kennedy-cislunar-space-the-next-military-frontier/.

Hitchens, T. (2019). *The Next Battlefield: Robots & AI In Cislunar Space*. Retrieved from https://breakingdefense.com/2019/09/the-next-battlefield-robots-ai-in-cislunar-space/

INCOSE (2007). *Systems Engineering Vision 2020*. Retrieved from http://www.ccose.org/media/upload/SEVision2020_20071003_v2_03.pdf

Krisciunas, K. and Schaefer, B. E. (1991). *A Model of the Brightness of Moonlight*. Publications of the Astronomical Society of the Pacific.

Lucey, J. R. *User's Guide to the Night Sky*. University of Durham. Retrieved from https://community.dur.ac.uk/john.lucey/users/lunar_sid_syn.html.

McLeary, P. and Hitchens, T. (2019). *US, Japan To Ink Hosted Payload Pact to Monitor Sats*. Retrieved from https://breakingdefense.com/2019/08/us-japan-to-ink-hosted-payload-pact-to-monitor-sats/

NASA (2009). *DSN Telecomunications Link Design Handbook.* Retrieved from https://deepspace.jpl.nasa.gov/dsndocs/810-005/.

NASA (2017). *Moon Fact Sheet.* Retrieved from https://nssdc.gsfc.nasa.gov/planetary/factsheet/moonfact.html/.

NASA (2019). *Earth Fact Sheet.* Retrieved from https://nssdc.gsfc.nasa.gov/planetary/factsheet/moonfact.html/.

"National Space Exploration Campaign Report," National Aeronautics and Space Administration (NASA) (September 18)

Naval Air Warfare Center (NAVWAR) (2013). *Electronic Warfare and Radar Systems.*

Office of the President of the United States (2018). Space Policy Directive 3. Washington, DC. Retreived from https://www.whitehouse.gov/presidential-actions/space-policy-directive-3-national-space-traffic-management-policy/

Ostman, J. A. (2019). *Cislunar Trajectory Generation with Sun-Exclusion Zone Constraints Using a Genetic Algorithm and Direct Method Hybridization*. Air Force Institute of Technology.

Parker, S. J. and Anderson, R. L. (2013) *Low-Energy Lunar Trajectory Design.* Pasadena, California: Jet Propulsion Laboratory. Retrieved from https://descanso.jpl.nasa.gov/monograph/series12/LunarTraj--Overall.pdf.

Pisacane, V. L. (2016) *The Space Environment and its Effects on Space Systems.* Reston, VA: American Institute of Aeronautics and Astronautics.

Regan, H. and Pokharel, S. (2019). *India is trying to reconnect with lost lunar lander on the surface of the moon.* Retreived from https://www.cnn.com/2019/09/09/asia/india-moon-landing-signal-intl-hnk-scli/index.html

Stahl, H. P., Stephens, K., Henrichs, T., Smart, C., & Prince, F. A. (2011). Update on parametric cost models for space telescopes. Optical Engineering, 49(7). http://doi.org/10.1117/1.3456582

Stern, J. L. and Wachtel, S. T. (2017). *Genetic Algorithm Optimization Of Geosynchronous Earth Orbit Space Situational Awareness Systems Via Parallel Evaluation Of Executable Architectures.* Air Force Institute of Technology.

Szebehely, V. (1967). *Theory of Orbits: The Restricted Problem of Three Bodies.* Academic Press: New York and London.

Thompson, A. (2020). *SpaceX Launches 60 Starlink Satellites, Nails Rocket Landing in Record-Breaking Flight*. Retrieved from https://www.space.com/spacex-starlink-2-launch-success.html

US Joint Chiefs of Staff (2018). Joint Publication 3-14 Space Operations. Washington DC. Retrieved from https://www.jcs.mil/Portals/36/Documents/Doctrine/pubs/jp3_14.pdf

Vallerie, E. M., III (1963) *Investigation of Photometric Data Received from an Artificial Earth Satellite.* Air Force Institute of Technology.

Vedda, J. A. (2018). *Cislunar Development: What to Build—And Why*. El Segundo, California: The Aerospace Corporation. Retrieved from https://aerospace.org/sites/default/files/2018-05/CislunarDevelopment.pdf

Wall, M. (2019). *This Is the Last Photo Israel's Beresheet Moon Lander Ever Took.* Retrieved from https://www.space.com/israel-moon-lander-beresheet-last-photo.html

Wiesel, W. E. (2010). *Spaceflight Dynamics*. Aphelion Press: Beavercreek OH.

Woodward, M., Cosgrove, D., Morinelli, P., Marchese, J., Owens, B., and Folta, D. (2011). *Orbit Determination of Spacecraft in Earth-Moon L1 and L2 Libration Point Orbits*. Astrodynamics Specialists Conference.

REPORT DOCUMENTATION PAGE

Form Approved
OMB No. 0704-0188

1. REPORT DATE *(DD-MM-YYYY)*	2. REPORT TYPE	3. DATES COVERED *(From - To)*
03/26/2020	Master's Thesis	Sept 2016 - Mar 2020

4. TITLE AND SUBTITLE
Evaluation Framework for Cislunar Space Domain Awareness (SDA) Systems

5a. CONTRACT NUMBER

5b. GRANT NUMBER

5c. PROGRAM ELEMENT NUMBER

6. AUTHOR(S)
Knister, Simon R., Capt USAF

5d. PROJECT NUMBER

5e. TASK NUMBER

5f. WORK UNIT NUMBER

7. PERFORMING ORGANIZATION NAME(S) AND ADDRESS(ES)
Air Force Institute of Technology
Graduate School of Engineering and Management (AFIT/EN)
2950 Hobson Way
Wright-Patterson AFB OH 45433-7765

8. PERFORMING ORGANIZATION REPORT NUMBER
AFIT-ENV-MS-20-M-221

9. SPONSORING/MONITORING AGENCY NAME(S) AND ADDRESS(ES)
Intentionally left blank

10. SPONSOR/MONITOR'S ACRONYM(S)

11. SPONSOR/MONITOR'S REPORT NUMBER(S)

12. DISTRIBUTION/AVAILABILITY STATEMENT
Distribution Statement A. Approved for public release; distribution unlimited.

13. SUPPLEMENTARY NOTES
This material is declared a work of the U.S. Government and is not subject to copyright protection in the United States.

14. ABSTRACT
Cislunar space is of increasing international interest, requiring expansion of existing Space Traffic Management (STM) functions. This research applies model-based systems engineering (MBSE) to assess performance and cost of a multiple cislunar SDA systems of systems. The test case architecture consists of a single satellite in an L1 Lyapunov orbit. Detection, track, and cost metrics are developed and physics of cislunar SDA are examined. Solar exclusion angles, solar phase angle, and lunar exclusion angles are play a large role in system performance. Lunar exclusion angles render ground-based observers useless. This research shows high utility for LEO constellations in the synodic plane.

15. SUBJECT TERMS
Space Domain Awareness (SDA), Cislunar astrodynamics, Model Based Systems Engineering (MBSE), Lunar logistics

16. SECURITY CLASSIFICATION OF:			17. LIMITATION OF ABSTRACT	18. NUMBER OF PAGES	19a. NAME OF RESPONSIBLE PERSON
a. REPORT	b. ABSTRACT	c. THIS PAGE			Lt Col Bryan D. Little, AFIT/ENY
U	U	U	UU	92	19b. TELEPHONE NUMBER *(Include area code)* (937) 255-6565 x4901 bryan.little@afit.edu